THE ARCTIC SYSTEM REANALYSIS, VERSION 2

D. H. Bromwich, A. B. Wilson, L. Bai, Z. Liu, M. Barlage, C.-F. Shih, S. Maldonado, K. M. Hines, S.-H. Wang, J. Woollen, B. Kuo, H.-C. Lin, T.-K. Wee, M. C. Serreze, and J. E. Walsh

The new regional 15-km Arctic System Reanalysis, version 2, provides the accuracy and details necessary for many Arctic climate studies over the period 2000–12.

The Arctic is in the midst of rapid change in its physical environment with pronounced increases in surface air temperature, especially for winter and spring over subarctic land areas (Serreze and Francis 2006; Screen et al. 2012), as well as over the Arctic Ocean (e.g., Comiso 2003; Kohnemann et al. 2017). Arctic sea ice extent has declined throughout the satellite era, with the record September minimum extent in 2012 (Fig. 1) and the smallest maximum extent in March 2017 (National Snow and Ice Data Center 2017). Sea ice cover has thinned dramatically (Kwok and Untersteiner 2011), as historical evidence suggests that the recent sea ice minima are unmatched across the Arctic back to 1850 (Walsh et al. 2017).

Spring snow-cover extents (SCE) over Eurasia and North America have significantly declined since 2005 (National Oceanic and Atmospheric Administration 2016), with Arctic SCE declining more rapidly than September minimum sea ice extent (e.g., approximately −18% for June over the period 1967–2016; Derksen et al. 2017). Subsurface warming of the permafrost has also been observed in borehole measurements (e.g., Romanovsky et al. 2010). The area of the Greenland Ice Sheet experiencing summer melt has increased, and in mid-July 2012 some 99% of the surface area was melting according to satellite observations, a highly unusual but not unique event (Nghiem et al. 2012). There has also been accelerated movement

of Greenland outlet glaciers and increased runoff to the ocean (e.g., Rignot et al. 2011) as Greenland remains the largest land ice mass contributor to sea level rise (Harig and Simons 2016). However, glacier loss in other areas such as the Gulf of Alaska and the Canadian Archipelago are also significant contributors to sea level rise (Harig and Simons 2016) and may not be recoverable this century (Lenaerts et al. 2013). The symptoms of accelerated Arctic climate change are seemingly pervasive (Intergovernmental Panel on Climate Change 2013).

These changes may represent early signs of the expected Arctic amplification of the effects of increasing greenhouse gases (e.g., Screen and Simmonds 2010). However, the Arctic climate system is also home to strong natural variability (Kay et al. 2011; Ding et al. 2017), such as that associated with the North Atlantic Oscillation, the Arctic Oscillation, the Pacific decadal oscillation, and other atmospheric patterns (Thompson and Wallace 2000; Rogers et al. 2001; Rigor and Wallace 2004; Hartmann and Wendler 2005; Overland and Wang 2005). Indeed, the increase in sea ice volume in 2013 following the record minimum raises questions concerning the resilience of the Arctic sea ice cover (Tilling et al. 2015). While there is some evidence that the signature of greenhouse gas forcing has emerged in the Arctic over the last few decades (Fyfe et al. 2013), continued research to separate the forced response from intrinsic variability is needed. There is growing need to improve polar prediction and observing capacity, exemplified by the most recent polar endeavor, the Year of Polar Prediction (YOPP; Jung et al. 2016). This internationally coordinated effort of intensive observing and modeling activities will improve representation of polar processes in models and refine derived satellite products, among other benefits.

The community has long relied on global atmospheric reanalyses to explore climate system behavior. These syntheses merge a wide variety of surface, atmospheric, and satellite remote sensing data into gridded analyses that are important resources for investigating Arctic climate change and accompanying variability during recent decades, most often since 1979 (e.g., Lindsay et al. 2014). There are nevertheless some important caveats to using global reanalyses for climate change assessment. While the use of a fixed data assimilation system and forecasting model eliminates spurious shifts in the output caused by model upgrades (e.g., Bengtsson and Shukla 1988), the reanalyses remain sensitive to changes in the observing system (e.g., Bengtsson et al. 2004a,b). For example, the European Centre for Medium-Range Weather Forecasts (ECMWF) interim reanalysis (ERA-Interim,

hereafter ERAI; Dee et al. 2011) has artificial temporal trends due to the assimilation of rain-affected radiances from satellite passive microwave observations. The National Aeronautics and Space Administration (NASA) Modern-Era Retrospective Analysis for Research and Applications (MERRA) (Rienecker et al. 2011) and the National Centers for Environmental Prediction (NCEP) Climate Forecast System Reanalysis (CFSR) (Saha et al. 2010) exhibit discontinuities associated with the start of the modern microwave sounder [Advanced Television and Infrared Observation Satellite (TIROS) Operational Vertical Sounder (ATOVS)] era (Cullather and Bosilovich 2011; Zhang et al. 2012). Major temporal discontinuities have been largely resolved in MERRA, version 2 (Gelaro et al. 2017). ERAI, MERRA, and CFSR showed significant errors in temperature, moisture, and wind speed in the lowest 800 m over the Arctic Ocean when compared to independent sounding observations (Jakobson et al. 2012).

The Arctic System Reanalysis (ASR) is a demonstration regional reanalysis for the greater Arctic (see Fig. 1) and an exercise well aligned with the goals of YOPP. ASR, version 2 (ASRv2), spans the region poleward of the headwaters of the major rivers that flow northward into the Arctic Ocean and help maintain the low salinity of its near-surface layer. In Eurasia, these rivers are the Ob, Yenisei, Lena, and Kolyma, while the Mackenzie is the largest such river in North America. Also the major oceanic storm tracks are included in the ASR domain. Particular attention has been paid to specifying realistic ocean and land surface conditions. Horizontal resolution is finer than the global reanalyses (35 km and coarser grids) and comparable time resolution is used. Optimal polar physics are used where possible. Currently, the period of assimilation is 2000–12, which starts with the launch of the NASA Earth Observing System satellite *Terra* (and later *Aqua*) that supplies several of the input datasets. As a result, ASR is particularly suitable for detailed investigations of near-surface characteristics during the period of rapid Arctic change but lacks the multidecadal perspective of the global reanalyses. Thus, these different reanalyses are complementary to each other. ASR, version 1 (ASRv1), at 30-km grid spacing was outlined by Bromwich et al. (2016); the present manuscript describes ASRv2 at 15-km grid spacing and illustrates its performance in relation to ASRv1 and ERAI.

PRODUCTION SYSTEM. *Polar WRF.* The regional forecast model used for ASRv2 is based on the Weather Research and Forecasting (WRF) Model, version 3.6.0 (Skamarock et al. 2008), utilizing the Advanced Research version of the WRF (ARW) solver for fully

compressible nonhydrostatic equations (Table 1). WRF has been optimized for polar environments (known as Polar WRF; http://polarmet.osu.edu/PWRF/) including improving the heat transfer through snow and ice (Hines and Bromwich 2008), the inclusion of fractional sea ice (Bromwich et al. 2009), the ability to specify variable sea ice thickness, snow depth on sea ice, and sea ice albedo (Hines et al. 2011, 2015; Wilson et al. 2011, 2012), and other optimizations included in the Noah land surface model (LSM; Barlage et al. 2010). With the aid of the Mesoscale and Microscale Meteorology Division at the National Center for Atmospheric Research (NCAR), many of these routines developed by the Polar Meteorology Group of the Byrd Polar and Climate Research Center at The Ohio State University are now part of the standard release of WRF (Powers et al. 2017; www.mmm.ucar.edu /weather-research-and-forecasting-model).

The ASRv2 domain is the same as ASRv1 (Bromwich et al. 2016), consisting of a one-way nest, with an outer domain covering most of the Northern Hemisphere (NH) that provides smooth meteorological fields at the lateral boundaries of the inner domain (Fig. 1). The inner domain covers approximately 1.2 × 10^8 km², or about 50% of the NH. Care has been taken to avoid placing the inner-domain boundaries across the highest topography ensuring a seamless transition of meteorological parameters. Polar WRF uses a staggered Arakawa C grid with 721 × 721 grid points on a polar stereographic projection and 15-km horizontal resolution for the inner domain. In the vertical direction, Polar WRF uses a terrain-following dry hydrostatic pressure coordinate system with 71 model levels and a constant pressure surface at the top of the model of 10 hPa. The lowest full model level is 4 m above ground level (AGL), with over 25 levels below 850 hPa, 0.5-km level

spacing in the midtroposphere, and approximately 0.8 km from the tropopause to the top of the model.

Initial and lateral boundary conditions for the outer domain in Polar WRF are provided by ERAI surface and upper-level model data. To avoid model drift in atmospheric circulation (Glisan et al. 2013; Hines et al. 2015), spectral nudging is implemented on temperature, geopotential height, and wind components above 100 hPa (top 20 vertical levels) on the inner domain (all levels in the outer domain). We use wavenumber 11 to impact only the large-scale synoptic conditions (wavelengths > 1,000 km), and setting the nudging coefficients for all three variables to 10 times the strength of ASRv1 removes additional upper-level model bias in the initial forecast. The top 8 km of Polar WRF are damped and the gravity wave drag option is selected to suppress gravity wave interference at the top of the model.

The physics parameterizations chosen for ASRv2 are based on extensive development and testing of Polar WRF over a wide range of Arctic environments including the Greenland Ice Sheet and the Arctic
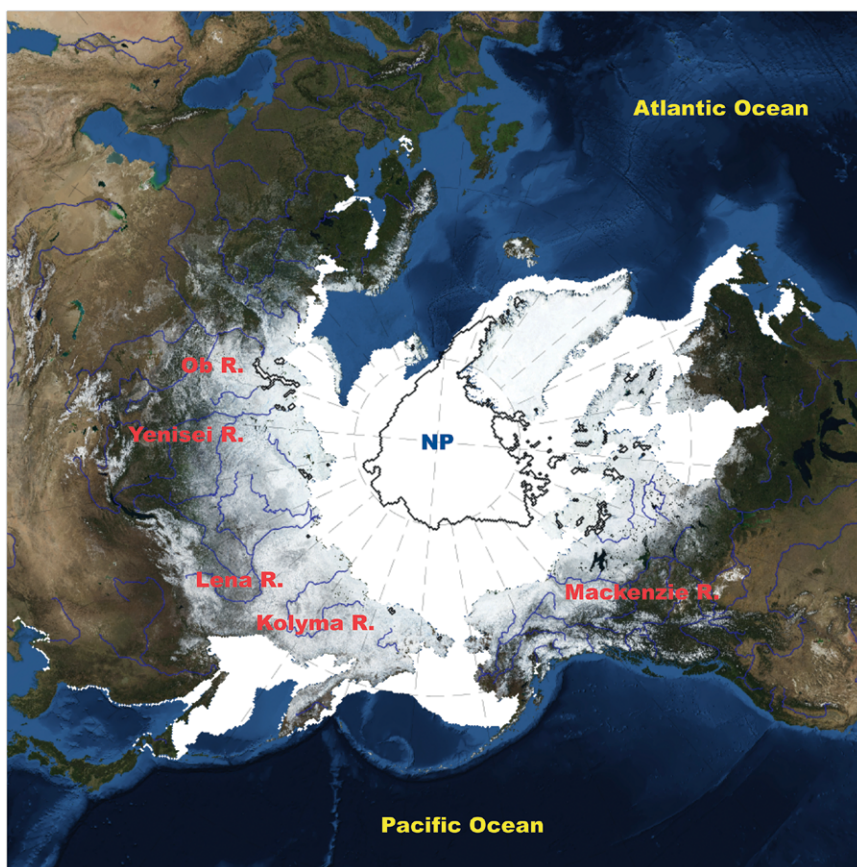

Fɪɢ. 1. Topographic relief map based on Blue Marble imaging (Stöckli et al. 2005) showing inner domain of ASRv2. River shapefiles produced by Natural Earth (naturalearthdata.com) and sea ice shapefiles produced by the National Snow and Ice Data Center (NSIDC; nsidc.org) showing maximum extent (white shading) in Mar 2012 and minimum extent (black line) in Sep 2012.

Ocean (Hines and Bromwich 2008; Bromwich et al. 2009; Hines et al. 2011; Wilson et al. 2011, 2012; Hines et al. 2015). The Goddard microphysics scheme is utilized for the cloud microphysics with ice, snow, and graupel processes represented (Tao and Simpson 1993; Tao et al. 2003). We use the Kain–Fritsch scheme (Kain and Fritsch 1990, 1993; Kain 2004) for the cumulus parameterization along with the climate-model-ready update to the global climate model (GCM) version of the Rapid Radiative Transfer Model (RRTMG) for longwave (LW) and shortwave (SW) radiation (Clough et al. 2005; Iacono et al. 2008). Different from ASRv1, however, we implement the new subgrid-scale cloud fraction interaction with radiation that allows for

Table 1. ASRv2 production system at a glance. An asterisk represents changes since ASRv1 (see text for details).	
Model	**Polar WRF 3.6.0***
Dynamical core	Fully compressible, Euler nonhydrostatic
Time-stepping scheme	Time-split integration using a third-order Runge–Kutta scheme
Vertical coordinate	Terrain-following, dry hydrostatic pressure
Horizontal resolution and grid	15 km*; Arakawa C grid staggered
Vertical resolution and model top	71 vertical levels: first level at 4 m, 25 levels below 850 hPa; 10-hPa top
Lateral boundary conditions	ERAI surface and upper-level model data; spectrally nudged above 100 hPa*
Physics parameterizations	
Microphysics	Goddard
Cumulus	Kain–Fritsch (with subgrid cloud fraction interaction with radiation*)
Radiation (SW and LW)	RRTMG
Planetary boundary layer and surface layer	MYNN 2.5
Data assimilation	**WRFDA 3.3.1 (3DVAR)**
Method	Dual outer loop;* 3-h cycle; assimilate observations within ±1.5 h of analysis
Background error	Computed for every month based on 12- and 24-h Polar WRF forecasts
Data	
Conventional data	NCEP Prepared Binary Universal Form for the Representation of Meteorological Data (PREPBUFR)
Sea surface winds	QuickSCAT and Special Sensor Microwave Imager (SSM/I)
Satellite radiances	AMSU-A, AMSU-B, Atmospheric Infrared Sounder (AIRS), MHS, High Resolution Infrared Radiation Sounder 3 and 4 (HIRS3 and HIRS4)
GPS	RO and IPW
Land surface model	**Noah LSM with High-Resolution Land Data Assimilation System (HRLDAS)**
Snow cover: depth and density	NCEP Final Analysis
Land surface albedo	MODIS updated every 8 days; Greenland updated daily
Orography	U.S. Geological Survey (USGS) Global 2-min-resolution (GTOPO 2′) digital elevation model (DEM); Greenland 1-km DEM (Bamber et al. 2001)
Vegetation	MODIS updated every 8 days
Soil	Initialized with ERAI soil temperature and moisture
Ocean conditions	**Prescribed (based on reanalysis and observations)**
SST	ERAI
Sea ice	
Concentration and thickness	Advanced Microwave Scanning Radiometer for Earth Observing System (AMSR-E) 6.25 km (summer 2002–11); alternative 25-km satellite-based products (2000–summer 2002, 2012) (Maslanik et al. 2007, 2011)
Albedo	Annually varying seasonal cycle based on melt and freeze date observations from satellite passive microwave measurements
Snow cover on sea ice	Seasonally varying

more realistic shortwave and longwave, improving additional weather parameters (Alapaty et al. 2012; Zheng et al. 2016). The Noah LSM (Chen and Dudhia 2001) and the Mellor–Yamada–Nakanishi–Niino (MYNN) (Nakanishi 2001; Nakanishi and Niino 2004, 2006) 2.5-level planetary boundary layer (PBL) and complementary surface-layer schemes are also utilized.

WRFDA system overview. NCAR's community WRF data assimilation (WRFDA, formerly WRF-Var) system is adopted for the component of atmospheric analysis in the ASR project. Over recent years, WRFDA has been extended to include a broad range of data assimilation (DA) techniques, including three- and four-dimensional variational data assimilation

FIG. 2. Snapshot coverage of nonradiance observations over the ASR domain within ±1.5-h time window centered at 0000 UTC 1 Jan 2007 including synoptic surface observations (black dots), METARs (purple plus signs), ship observations (royal blue dots), buoys (navy blue dots), radiosondes (purple asterisks), global positioning system refractivity observations (red dots), wind profiler (yellow dots), aviation in-flight weather reports (green dots), QuikSCAT sea surface winds (orange dots), and satellite atmospheric motion vectors (aqua dots).

(3DVAR and 4DVAR) and hybrid ensemble–variational (EnVar) approaches (Huang et al. 2009; Barker et al. 2012). ASR uses the 3DVAR technique that was more mature than other schemes (4DVAR and hybrid EnVar) in WRFDA at the time the project was originally proposed. WRFDA-3DVAR is based upon the fifth-generation Pennsylvania State University–National Center for Atmospheric Research Mesoscale Model (MM5) 3DVAR system (Barker et al. 2004), but the basic software framework is fully updated for ARW (Skamarock et al. 2008). It has been successfully implemented for operational/real-time applications at several numerical weather prediction centers and research institutes (Barker et al. 2012), including the Antarctic Mesoscale Prediction System (Powers et al. 2012).

WRFDA produces analyses of surface pressure and 3D atmospheric temperature, moisture, and wind fields on the WRF Model grid by assimilating many types of observations, including most conventional (both surface and upper air) and remote-retrieval observations as well as radiance data from a number of satellite platforms (Barker et al. 2012). [For a more detailed description of WRFDA, see Skamarock et al. (2008).] All observations used in ASR are provided by NCEP in the binary universal form for the
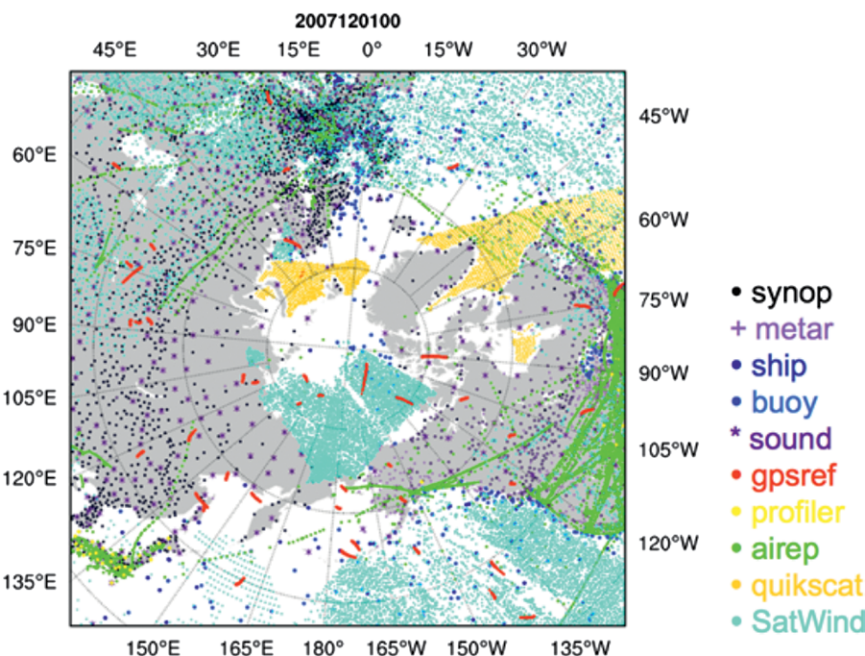
representation of meteorological data (BUFR) format. Figure 2 shows the typical coverage of nonradiance observations used in the ASR within a ±1.5-h data assimilation time window. High-latitude Arctic regions as well as ocean areas are sparsely monitored by conventional observations. Instead, nonradiance observations here are largely satellite atmospheric motion vectors and GPS radio occultation observations (assimilated as refractivity) providing upper-air information along with surface ocean winds (at 10 m) from the Quick Scatterometer (QuikSCAT).

SATELLITE RADIANCE ASSIMILATION. In addition to those non-radiance observations, radiance data from 12 microwave sensors [6 Advanced Microwave Sounding Unit (AMSU)-A, 3 AMSU-B, and 3 Microwave Humidity Sounder (MHS)] on board 7 polar-orbiting satellites, which have been proven to have a large positive impact on global medium-range forecast performance (e.g., Bouttier and Kelly 2001) and tropical storm forecasting using WRF (e.g., Liu et al. 2012; Schwartz et al. 2012), are also assimilated in ASR. Radiance observations are the major data source providing vertical temperature and moisture soundings over those regions with sparse conventional data coverage. For ASR, only the

channels 5–9 (temperature sensitive) of AMSU-A and the channels 3–5 (moisture sensitive) of AMSU-B/MHS are used. High-peaking and surface-sensitive channels are not used because of the relatively low ASR model top (10 hPa) and inaccurate input of surface emissivity and skin temperature. Figure 3 depicts the time series over a period of 13 years (2000–12) of global statistics of bias (left panels) and standard derivation (right panels) of observed minus calculated brightness temperatures using the Community Radiative Transfer Model (CRTM) (Han et al. 2006) with ERAI as input for AMSU-A channels 5–9. These monitoring statistics were obtained using WRFDA's "offline" variational bias correction (VarBC) option as described by Auligné et al. (2007) and Liu et al. (2012).

The starting dates from which radiance data become available are marked in Fig. 3 for the different instruments. The only sensor covering the whole ASR period is *NOAA-15* AMSU-A. Monitoring statistics are a powerful tool for identification of bad channels within the lifetime of sensors, which have to be blacklisted in the data assimilation. For instance, *Meteorological Operational-2* (now known as *MetOp-B*) AMSU-A channel 7 had a substantially increased standard deviation from January 2009 onward, which was known to suffer from increasing instrument noise and was turned off by operational data assimilation systems. The jump of both bias and standard deviation for *NOAA-19* AMSU-A channel 8 can also be clearly seen from Fig. 3. The radiance blacklist table used in ASR is
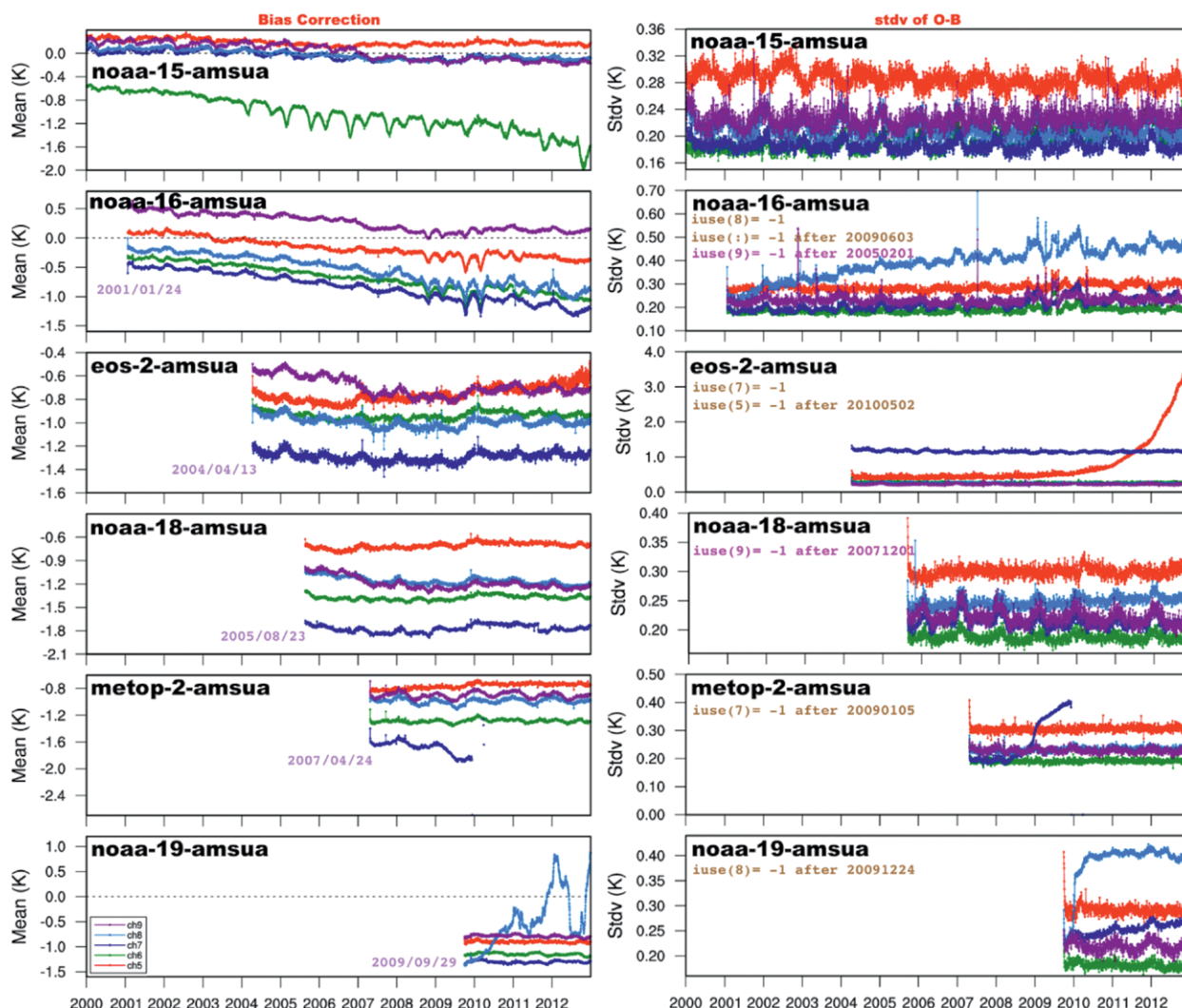
FIG. 3. Time series over a period of 13 years (2000–12) of global statistics of (left) bias and (right) standard deviation of observed minus CRTM-calculated brightness temperatures with ERAI as input, for AMSU-A channels 5–9 from six satellites. The dates marked in the left panels are the starting dates from which the corresponding radiance data became available. Also listed in the right panels is an important blacklist of radiance channels (see text).

a combination of our monitoring results and blacklist tables used by NCEP operations (see www.emc.ncep .noaa.gov/mmb/data_processing/Satellite_Historical _Documentation.htm) and ERAI (P. Poli 2012, personal communication). Some important radiance blacklist decisions in ASR are marked in the right panel of Fig. 3. For instance, iuse(:) = −1 means all channels are turned off, and iuse(8) = −1 denotes that channel 8 is not used. It is evident that radiance bias characteristics of different channels have been evolving with time and exhibit, to a different extent, seasonal variations, posing the need for a time-evolving and adaptive bias correction scheme. A state-of-the-art VarBC scheme was implemented in WRFDA and used for ASR, which is similar to that used at NCEP (Derber and Wu 1998) and ECMWF (Dee and Uppala 2009). Offline monitoring statistics also provide pretrained bias correction coefficients for individual channels, which are used as the initial condition of the cycling VarBC scheme in different streams of ASR production runs and can minimize the spinup effect of bias correction adjustment (Liu et al. 2012; Schwartz et al. 2012).

SURFACE OBSERVATION ASSIMILATION. WRFDA does not directly analyze the screen-level atmospheric parameters (i.e., temperature T and moisture Q at 2 m and wind at 10 m), which are important variables commonly used for climate trend analysis. Instead, WRFDA analyzes atmospheric variables at the lowest model level by assimilating 2-m temperature and moisture and 10-m zonal (U) and meridional (V) wind observations from surface stations [surface synoptic observations (SYNOP), aviation routine weather reports (METAR), ship observations (SHIP), buoy observations (BUOY)]. The lowest model level of the ASR domain is at about 4 m, which allows 10-m-wind analysis accurately derived from a vertical interpolation and 2-m T and Q analysis extrapolated using the model's local lapse rate. To account for the difference between model terrain and surface station elevation, terrain corrections are applied to surface observations (also including surface pressure) before they are assimilated. Note that 2-m temperature and moisture and 10-m U and V wind are the diagnostic, not prognostic, variables in the WRF Model. Therefore, their analyses do not affect the subsequent WRF Model forecast during the ASR data assimilation/forecast cycles.

ATMOSPHERIC BACKGROUND ERROR COVARIANCES. Another important aspect is the background error covariance (BEC) statistics that constrain (together with observation errors) the weight between the model background (i.e., a 3-h forecast from previous cycle's analysis) and the observations and also propagate information from observed to unobserved areas/variables in both the horizontal and vertical through spatial and multivariate correlations implied in the BEC. BECs for ASR were generated using the so-called National Meteorological Center (NMC) method (Parrish and Derber 1992), which takes differences between forecasts of different lengths valid at common times. ASR uses the differences between the 24- and 12-h WRF forecasts, initialized from ERAI interpolated into the ASR grid and valid at either 0000 or 1200 UTC over different months.

LAND SURFACE. *Data assimilation.* Land surface models coupled to mesoscale meteorological models have been shown to perform poorly during cold-season processes, such as snowpack physics and soil heat diffusion, leading to an inadequate representation of spring snowmelt timing and the soil temperature profile, two major metrics of climate change in the Arctic (Slater et al. 2007; Pan et al. 2003; Barlage et al. 2010). Addressing these model issues through data assimilation into land surface models is limited by the paucity of quality state variables at high latitudes. In the ASR, several existing global-scale satellite observations have been identified to improve the representation of the land surface. These data are either integrated directly into the model or used to develop new datasets consistent with the Noah land model infrastructure.

Currently in the WRF–Noah model, land surface properties, such as green vegetation fraction and albedo, are prescribed climatological values based on historical Advanced Very High Resolution Radiometer (AVHRR) satellite data. With the launch of the Moderate Resolution Imaging Spectroradiometer (MODIS) sensors on board the NASA *Terra* and *Aqua* platforms in 1999 and 2002 and real-time vegetation monitoring by the National Oceanic and Atmospheric Administration/National Environmental Satellite, Data, and Information Service (NOAA/NESDIS), the availability of high-spatial- and high-temporal-resolution remotely sensed land surface properties improved substantially. The primary concern in assimilating a wide variety of products is that they are consistent. For example, surface albedo is tightly coupled to snow cover so the system must consider this.

MODIS albedo. The Noah land surface model treats albedo as a mixture of snow-free and snow-covered surfaces with the weighting based on model-diagnosed snow-cover fraction. Satellite-based albedo observations are a combination of all surfaces present in the observation pixel. To use the satellite albedo

within the Noah LSM, a disaggregation must be done, since the Noah LSM requires both a snow-covered and snow-free albedo regardless of the presence of snow. The Noah LSM also requires a snow-cover and snow-free albedo everywhere at all times (e.g., snow-covered albedo in the tropics).

Two new time-varying albedo datasets are created for snow-free and snow-covered surfaces using the MODIS 8-day 0.05° global albedo product (MODIS product code MCD43C3; Schaaf et al. 2002) along with the MODIS snow-cover products (MOD10C2/MYD10C2; Hall et al. 2002). The MODIS data are first filtered using the albedo product-quality flag and then using the snow product "cloud obscured" flag (data are rejected if cloud cover is greater than 80%). To determine the snow-covered albedo, the MODIS snow products must report at least 70% snow cover on the non-cloud-covered portion. Likewise, to be considered snow free, snow cover must be less than 10%. Since only one albedo observation is used to determine two necessary model inputs, a forward-in-time and backward-in-time filling procedure is done using the nearest (in time) quality observation of either snow-covered or snow-free albedo for each global location. The resulting product for 2007 over a north Alaskan grid point (68.8°N, 154.9°W) is shown in Fig. 4. These albedo products have been produced for 2000–12.

Investigation of the above MODIS albedo (MCD43C3) over Greenland showed an unusual and unrealistic albedo time series. After analyzing a daily albedo dataset based on the MODIS daily snow-cover product (MOD10A1/MYD10A1; Hall et al. 2002), the ASR albedo assimilation replaced the MCD43C3-based product with the MOD10A1-based product over the permanent ice portions of Greenland.

NOAA/NESDIS green vegetation fraction. A real-time dataset of green vegetation fraction is produced weekly in near–real time by NOAA/NESDIS (Jiang et al. 2008). This dataset is available for the entire ASR processing period at 0.144° spatial resolution. This product is consistent with the current vegetation fraction data used in Noah. Therefore, no further parameter tuning is needed when using this product other than to reset the maximum and minimum annual vegetation fraction range.

DATA ACCESS. ASRv2 data are available from the NCAR Computational Information Systems Laboratory (CISL) Research Data Archive (NCAR/UCAR/OSU 2017).

EVALUATION. *Surface.* We compare near-surface variables from ASRv1, ASRv2, and ERAI
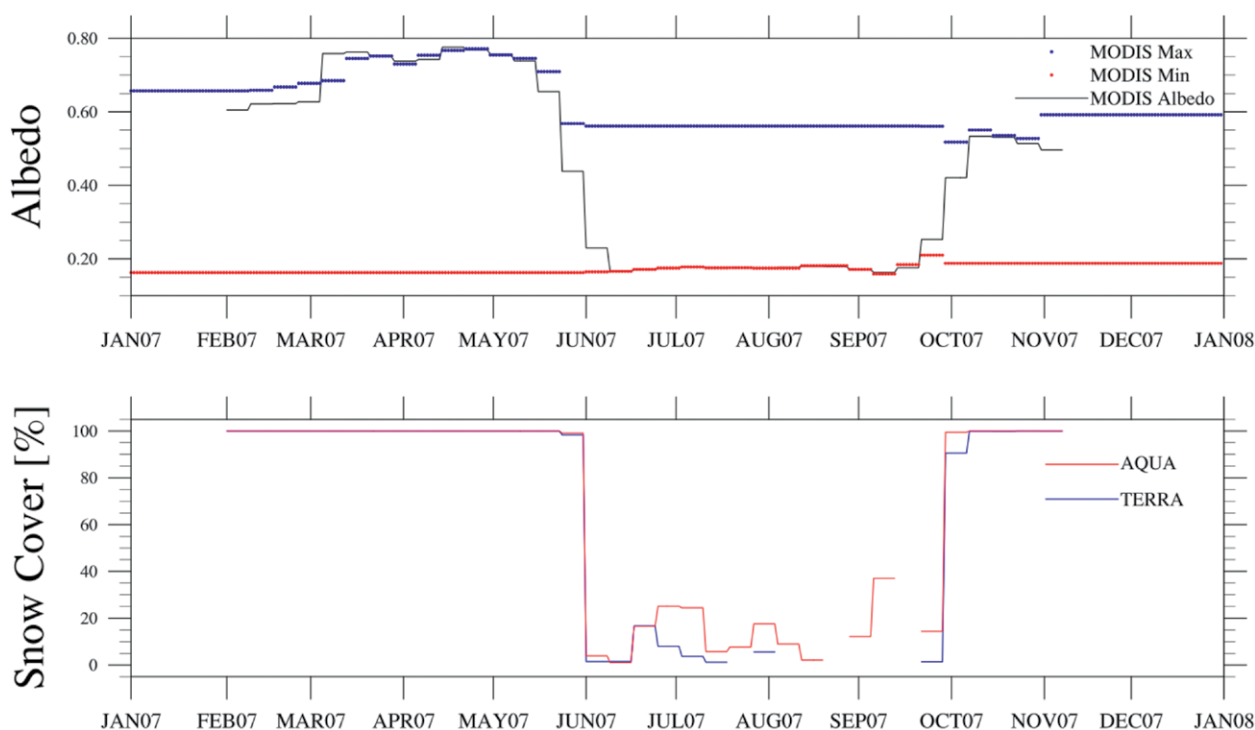

Fig. 4. Example gridpoint (top) ASRv2 time-varying snow-covered maximum albedo (blue dots) and snow-free minimum albedo (red dots) generated from the MODIS albedo product (black solid line) and (bottom) MODIS snow-cover products. Example time series are shown for 2007 over a north Alaska grid point (68.8°N, 154.9°W).

to observations from ~5,000 surface stations provided by the National Centers for Environmental Information (www.ncdc.noaa.gov/; counts vary by UTC hour, season, and year) and the Greenland Climate Network (GC-Net; http://cires1 .colorado.edu/steffen/gcnet/) for the period January 2000–December 2010 to compare the broadscale performance of ASR at increasing horizontal resolution (Table 2; from 80 km for ERAI to 15 km for ASRv2). All observed time series were screened for outliers and discontinuities. The results reflect reanalysis performance at 3-h intervals in relation

to surface observations that are mostly assimilated (except for GC-Net stations), and therefore are not entirely independent. Reanalysis values are spatially interpolated to the station locations from the surrounding four grid points. ASR is available every 3 h while the ERAI is linearly interpolated between analysis times (0000, 0600, 1200, and 1800 UTC) to produce intermediate values (at 0300, 0900 UTC, etc.). Table values are 11-yr averages for each month derived from averaging the results for all 5,000 stations. Lower bias, smaller root-mean-square error (rmse), and higher correlation show a better fit of
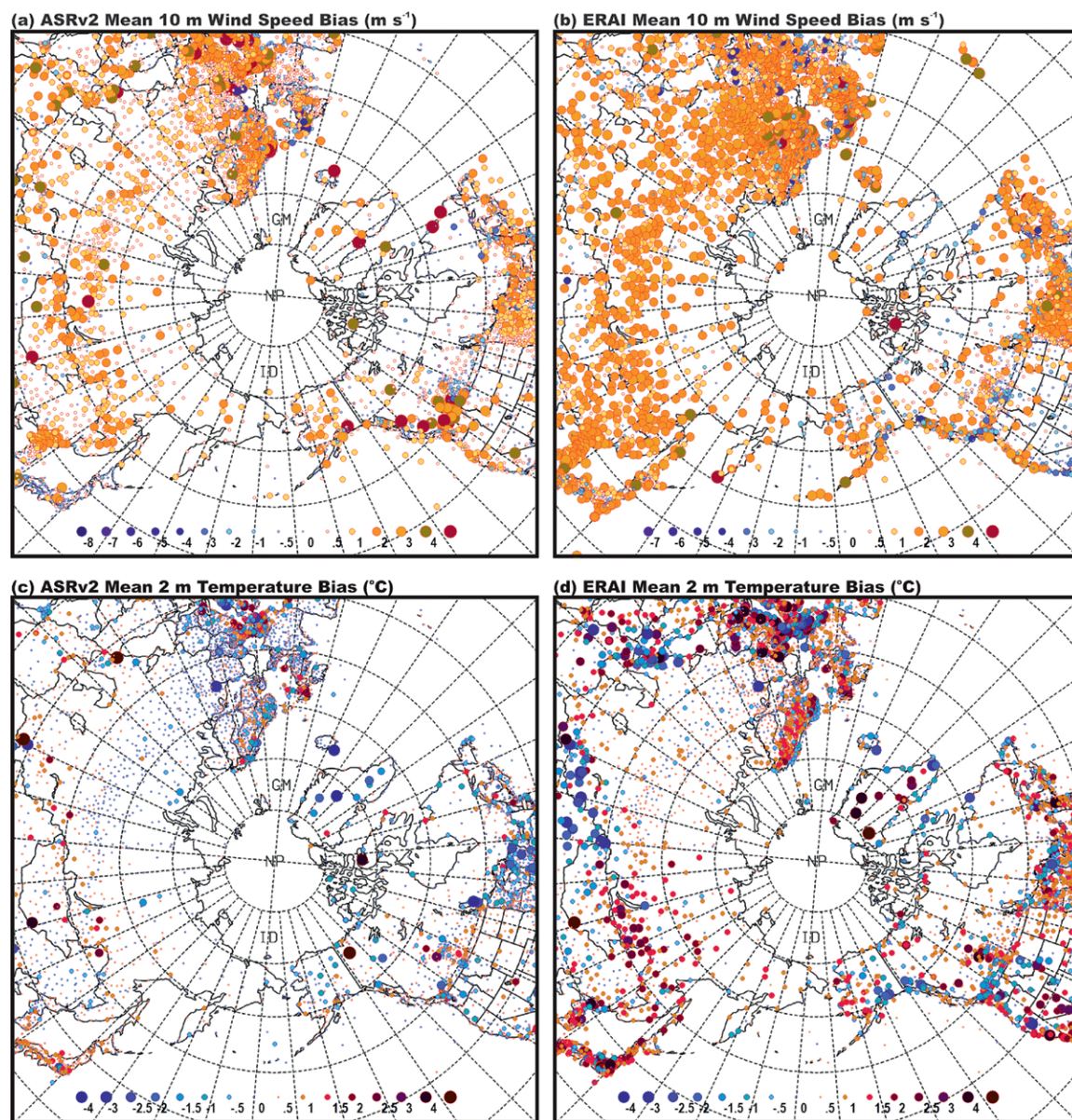

Fɪɢ. 5. Annual-mean biases for the period 2000–10 for the (left) ASRv2 and (right) ERAI for (a),(b) 10-m wind speed (m s⁻¹) and (c),(d) 2-m temperature (°C). Magnitudes of the biases are given by the color scale and the size of the symbol.

TABLE 2. Long-term monthly and annual–mean bias, rmse, and correlation for ERAI, ASRv1, and ASRv2 for 2000–10.

Month	Bias			Rmse			Correlation		
	ERAI	ASRv1	ASRv2	ERAI	ASRv1	ASRv2	ERAI	ASRv1	ASRv2
10-m wind speed (m s⁻¹)									
Jan	0.70	−0.06	0.39	2.36	1.92	1.55	0.67	0.71	0.80
Feb	0.57	−0.08	0.38	2.27	1.90	1.56	0.67	0.71	0.80
Mar	0.40	−0.19	0.27	2.22	1.89	1.50	0.67	0.73	0.82
Apr	0.21	−0.31	0.20	2.11	1.82	1.48	0.65	0.72	0.81
May	0.18	−0.35	0.19	2.04	1.77	1.38	0.62	0.69	0.81
Jun	0.20	−0.29	0.21	1.97	1.70	1.33	0.60	0.67	0.79
Jul	0.25	−0.27	0.23	1.93	1.65	1.30	0.58	0.65	0.78
Aug	0.30	−0.22	0.25	1.92	1.63	1.28	0.59	0.65	0.78
Sep	0.46	−0.17	0.29	2.03	1.68	1.36	0.63	0.69	0.79
Oct	0.54	−0.16	0.28	2.15	1.75	1.41	0.66	0.71	0.80
Nov	0.59	−0.15	0.34	2.26	1.84	1.47	0.66	0.71	0.81
Dec	0.66	−0.10	0.36	2.34	1.92	1.53	0.66	0.70	0.80
Grand mean	0.42	−0.19	0.28	2.13	1.79	1.43	0.64	0.69	0.80
2-m temperature (°C)									
Jan	0.37	0.15	−0.01	2.15	1.52	1.24	0.92	0.96	0.97
Feb	0.34	0.07	−0.06	2.13	1.42	1.22	0.92	0.96	0.97
Mar	0.28	0.05	−0.11	2.04	1.33	1.08	0.93	0.96	0.97
Apr	0.24	0.08	−0.04	1.99	1.26	0.96	0.92	0.96	0.97
May	0.22	0.06	−0.07	1.99	1.27	1.08	0.92	0.96	0.97
Jun	0.23	0.06	−0.08	1.97	1.36	1.08	0.91	0.95	0.97
Jul	0.26	0.03	−0.11	1.94	1.30	1.07	0.90	0.95	0.96
Aug	0.27	0.06	−0.08	1.89	1.27	1.04	0.90	0.95	0.97
Sep	0.27	0.10	−0.05	1.86	1.25	1.05	0.92	0.96	0.97
Oct	0.30	0.15	−0.01	1.84	1.25	1.05	0.92	0.96	0.97
Nov	0.36	0.25	0.04	1.93	1.43	1.07	0.92	0.96	0.97
Dec	0.40	0.25	0.07	2.09	1.53	1.18	0.92	0.96	0.97
Grand mean	0.29	0.11	−0.04	1.98	1.35	1.09	0.92	0.96	0.97
2-m dewpoint temperature (°C)									
Jan	0.61	0.19	0.00	2.34	2.06	1.86	0.92	0.94	0.95
Feb	0.56	0.05	0.11	2.33	1.98	1.88	0.91	0.94	0.94
Mar	0.45	0.01	0.09	2.30	1.86	1.68	0.91	0.94	0.95
Apr	0.32	−0.03	0.09	2.24	1.78	1.47	0.88	0.93	0.95
May	0.11	−0.19	0.11	2.12	1.70	1.50	0.87	0.92	0.93
Jun	−0.12	−0.38	0.17	2.00	1.74	1.46	0.85	0.90	0.92
Jul	−0.22	−0.05	0.27	1.90	1.59	1.42	0.82	0.88	0.91
Aug	−0.17	−0.20	0.23	1.86	1.58	1.39	0.84	0.89	0.92
Sep	−0.03	−0.28	0.13	1.85	1.60	1.42	0.89	0.92	0.94
Oct	0.12	−0.04	0.07	1.87	1.58	1.43	0.91	0.94	0.95
Nov	0.33	0.07	0.00	2.02	1.79	1.47	0.92	0.94	0.96
Dec	0.55	0.17	−0.04	2.26	2.00	1.66	0.92	0.94	0.95
Grand mean	0.21	−0.06	0.10	2.09	1.77	1.55	0.89	0.92	0.94

Month	Bias			Rmse			Correlation		
	ERAI	ASRv1	ASRv2	ERAI	ASRv1	ASRv2	ERAI	ASRv1	ASRv2
Surface pressure (hPa)									
Jan	0.11	0.05	0.05	1.06	0.91	0.80	0.99	0.99	0.99
Feb	0.11	0.06	0.01	1.01	0.88	0.80	0.99	0.99	0.99
Mar	0.04	0.06	0.01	0.98	0.86	0.76	0.99	0.99	0.99
Apr	−0.02	0.01	−0.05	0.92	0.83	0.71	0.99	0.99	0.99
May	−0.08	0.00	−0.10	0.89	0.80	0.70	0.99	0.99	0.99
Jun	−0.14	0.01	−0.11	0.88	0.79	0.68	0.98	0.99	0.99
Jul	−0.18	0.01	−0.11	0.87	0.76	0.67	0.98	0.98	0.98
Aug	−0.15	0.01	−0.09	0.86	0.76	0.66	0.98	0.98	0.99
Sep	−0.06	0.02	−0.05	0.90	0.81	0.71	0.98	0.99	0.99
Oct	0.01	0.03	−0.07	0.91	0.81	0.75	0.99	0.99	0.99
Nov	0.07	0.05	0.02	0.96	0.85	0.74	0.99	0.99	0.99
Dec	0.11	0.06	0.05	1.03	0.90	0.78	0.99	0.99	0.99
Grand mean	−0.01	0.03	−0.04	0.94	0.83	0.73	0.99	0.99	0.99

TABLE 2. Continued.

the reanalysis to the observed time series. The 11-yr mean is very similar to that obtained for each year.

Annual-mean 10-m wind speed biases are smaller in the ASR products compared to ERAI, though a positive (negative) bias is demonstrated by ASRv2 (ASRv1). The annual spatial distribution of 10-m wind speed bias at the observation sites (Fig. 5) shows that ASRv2 almost everywhere has a reduced bias in comparison to ERAI, apart from Scandinavia, Europe, and the U.S. Midwest. Terrain variations not well resolved at 15 km (Fig. 1) may be partly responsible for the reanalysis challenges in Scandinavia and Europe. Table 2 reveals that there is a substantial improvement in rmse and correlation between ERAI and ASRv2, where ASRv2 captures two-thirds of the 3-hourly wind speed variance. Performance is better in summer than winter when the speeds are higher. As described in Bromwich et al. (2016), the improvements in near-surface wind are tied to the finer resolution in ASR and the improved skill in capturing local wind effects near complex terrain. ASRv1 (30 km) wind fields have been shown to be well represented, including wind related to topographically forced wind events (Moore et al. 2016) and Arctic cyclones (Tilinina et al. 2014). The present results along with Moore et al. (2016) for ASRv2 demonstrate that local wind effects are even better captured by ASRv2 at 15-km resolution. (See "Nares Strait flow" sidebar.)

Analysis reveals that ERAI and ASR products have small annual-mean 2-m temperature biases, with the smallest biases represented by ASRv2. However,

ASRv2 is colder than both ASRv1 and ERAI with small negative biases from January through October. However, these biases are well within the statistical error inherent in the model version change between ASRv1 and ASRv2. The annual spatial bias (Fig. 5) confirms the bias magnitude reduction in ASRv2 in comparison to ERAI except in the same problematic areas as for wind speed (Scandinavia, Europe, and U.S. Midwest). Nearly halving the annual-mean rmse value from ERAI to ASRv2 (Table 2) indicates that ASRv2 shows a much closer fit to the observations and the standard deviation of unexplained variance is small. This is further supported by the increasing skill indicated by higher correlation.

Annual-mean 2-m dewpoint biases are similar between the reanalyses. Negative monthly dewpoint biases but small positive 2-m temperature biases for ASRv1 from April through October indicate drier than observed conditions. Negative 2-m temperature biases but positive dewpoint biases during the summer months in ASRv2 reflect ample moisture due to the improved cloud processes implemented in ASRv2. Again, lower annual-mean rmse and higher correlation in ASRv2 show an improvement in overall fit and skill.

All three reanalyses capture the surface pressure (atmospheric circulation) very well with very small biases, low rmses, and very high correlations. Consistent with other near-surface variables, the rmse decreases from ERAI to ASRv2. To summarize, ASRv2 at 15 km shows a close fit to the surface

observations throughout the year with the "large-scale parameter" surface pressure being the most skillful and the "more localized parameter" surface wind speed being less so.

Upper air. For analysis of the upper-air variables in ASRv2, we have selected 500-hPa temperature and 700-hPa relative humidity for comparison with ERAI for the period December 2006–November 2007 (Fig. 6). Figure 6a shows the annual-mean 500-hPa temperature in ASRv2. The pattern aligns closely with the expected mean large-scale circulation. The coldest temperatures are located in the vicinity of the largest troughs, centered over Canada (~75°W) and Siberia

(~140°E). A weaker trough is indicated over eastern Europe (~45°E) as well, with the strongest gradients throughout the midlatitudes within the major troughs. Figure 6b shows the differences between ASRv2 and ERAI, which are generally within ±0.1°C. This is similar to the radiosonde comparison conducted by Bromwich et al. (2016) for ASRv1 and ERAI. The differences do not reveal systematic biases with scattered differences likely tied to small local variations between the reanalyses' assimilations. The greatest differences occur throughout the North Pacific, North Atlantic, and in areas of complex terrain.

Relative humidity at 700 hPa illustrates the midtroposphere (~3,000 m), which is the level at

NARES STRAIT FLOW

Strong low-level winds are a common cold-season feature in Nares Strait, located between the high terrain of Greenland and Ellesmere Island (Samelson and Barbour 2008). The strong ageostrophic winds are due to orographic channeling down the pressure gradient between high pressure over the Arctic Ocean (Lincoln Sea) and low pressure over Baffin Bay. They may play a key role in generating the persistent winter

North Water polynya in northern Baffin Bay. Samelson and Barbour (2008) modeled these winds with Polar MM5 (predecessor to Polar WRF) with a resolution of 6 km. Figure SB1 shows an example of these events that occurred on 9 February 2007 captured by the ASRv1 and ASRv2. The 15-km ASRv2 does a much better job resolving the orography of Nares Strait, and thus the winds are much stronger (>20 m s^{-1}) and

more continuous than at the 30-km resolution (~15 m s^{-1}). The katabatic winds over Greenland feed into the wind flow at two locations in ASRv2. Notice the multiple centers in the low over Baffin Bay compared to the single center in ASRv1. The high over the Arctic Ocean is more clearly captured by the 15-km ASRv2. This case illustrates that topographically forced winds are much better captured by the finer resolution of ASRv2.
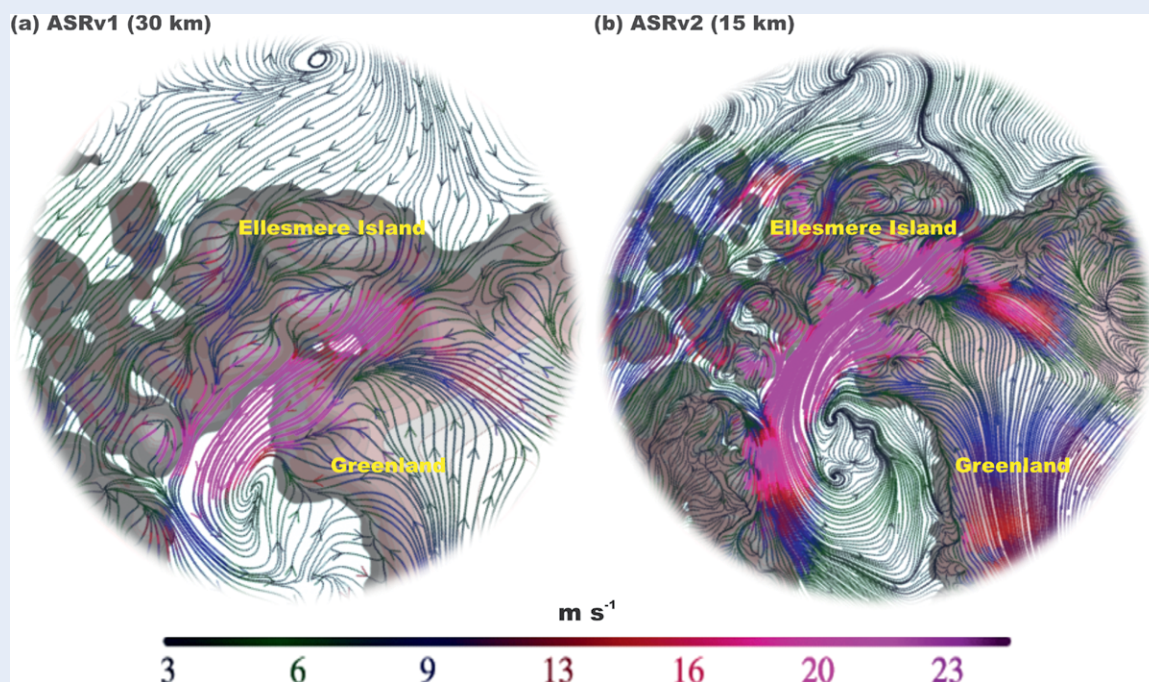

Fɪɢ. SB1. Streamlines and wind speeds (colors) at 10-m for an intense orographically channeled wind event in Nares Strait on 9 Feb 2007 as captured by (a) ASRv1 and (b) ASRv2.

which most weather systems are steered across the NH. Figure 6a depicts the annual-mean relative humidity for December 2006–November 2007 showing a general low-to-high-latitude gradient. The lowest relative humidity is found in the arid desert regions of the U.S. Southwest (30°–35°N, 110°–125°W) and the Middle East (30°N, 50°E) and near the influence of the subtropical high in the Pacific. Higher relative
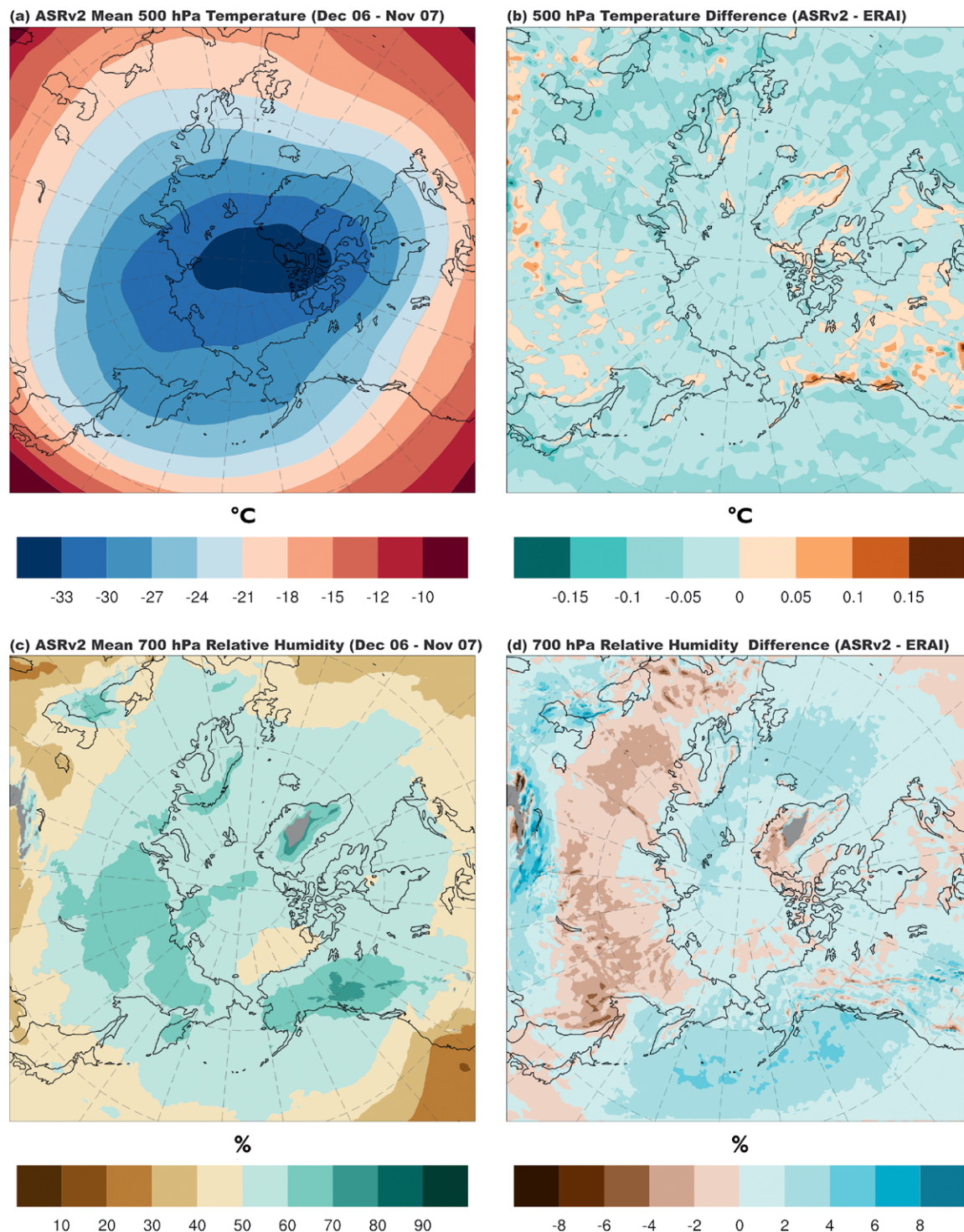

Fɪɢ. 6. (a) ASRv2 mean 500-hPa temperature (°C), (b) difference between ASRv2 and ERAI for 500-hPa temperature (°C), (c) ASRv2 mean 700-hPa relative humidity (%), and (d) difference between ASRv2 and ERAI for 700-hPa relative humidity (%) for the period Dec 2006–Nov 2007. Areas where the 700-hPa pressure level exists below ground based on the annual-average surface pressure have been masked in gray.

humidity north of 40°N is associated with the major NH storm tracks and cooler cloudier environments. The onshore flow along the west coast of North America (55°–65°N, 115°–165°W) is highlighted by the higher relative humidity in this location, along with areas in southwest Greenland (60°–65°N, 30°–45°W) and western Scandinavia (60°–70°N, 5°–40°E) and across Siberia (55°–70°N, 75°–165°E). An area of slightly lower relative humidity is located in the vicinity of the Beaufort Sea high (70°–80°N, 110°W–180°), which was exceptionally strong during this period and has been linked to a number of teleconnections and summer sea ice decline (L'Heureux et al. 2008; Serreze and Barrett 2011). Figure 6d shows the differences between ASRv2 and ERAI, where magnitudes are generally within ±4%. ASRv2 has higher relative humidity across the main oceanic storm-track regions of the North Pacific and Atlantic and smaller positive differences compared to ERAI across much of the Arctic. ASRv2 demonstrates lower relative humidity across much of the continental areas of Eurasia. Compared to the ASRv1 analysis with radiosondes (Bromwich et al. 2016), these results are comparable to an average 2% deficit in the RH across the domain with slightly higher RH in ASRv2 than ERAI.

Precipitation. We compare ASRv2 mean annual total forecast precipitation to ERAI for the 2000–10 period (Fig. 7). ASRv2 mean precipitation (Fig. 7a) clearly depicts the major storm tracks of the North Pacific and Atlantic where over 2,000 mm of annual precipitation falls. Greater amounts are also shown along the higher terrain of western North America. Much lighter amounts (<600 mm) fall across much of the Arctic basin and in the desert regions of the Middle East. Figure 7b shows that differences between ASRv2 and ERAI across much of the domain are generally ±10%. Both storm-track regions show up to 10% less annual precipitation in ASRv2 than in ERAI. The greatest differences between the two reanalyses occur over the highest terrain in western North America, the higher elevations throughout central Asia, and Greenland where differences are in excess of 50%. Across much of the Arctic, differences are small, though ASRv2 is dry (~15%) relative to ERAI throughout much of the western Arctic basin.

To evaluate monthly and seasonal characteristics of precipitation in ASRv2 and improvements over ASRv1, we repeat our analysis from Bromwich et al. (2016; ASRv1 included here for comparison) for the period December 2006–November 2007 using the Global Historical Climatology Network, version 2 (GHCN2) (Peterson and Vose 1997), and the Adjusted

Historical Canadian Climate Data (AHCCD) (Mekis and Hogg 1999) precipitation gauges (Fig. 7a). Each has undergone quality-control procedures to improve wind undercatch, evaporation, and adjustments for trace observations, all particularly important for Arctic precipitation (Peterson and Easterling 1994; Easterling and Peterson 1995; Mekis and Hopkinson 2004; Mekis 2005; Devine and Mekis 2008). We used only stations with complete annual records and divided the analysis between midlatitude (south of 60°N; 296 stations) and polar (north of 60°N; 78 stations).

Compared to the midlatitude stations (Fig. 7c), we note further improvements in the summertime precipitation for this particular season (summer 2007). Monthly biases for April–July are smaller in ASRv2 than in ASRv1 (10%–15%), though still generally overpredicted and higher than those demonstrated by ERAI. While warm-season precipitation is well captured by ASRv2, the cooler season shows drier biases in ASRv2 from August through March. For the polar stations (Fig. 7d), ASRv2 is comparable to ERAI from March through October. Significant improvements over ASRv1 (>10%) occur during the warmer months of May–August. Similar to the midlatitudes; however, the months of November–February are generally drier in ASRv2 than in ASRv1 or ERAI.

Downward radiation at the surface. Annual-mean incident SW and downwelling LW from Clouds and the Earth's Radiant Energy System Energy Balance and Filled (CERES-EBAF; Loeb et al. 2009; Kato et al. 2013) monthly 1° × 1° dataset are compared to ASRv2 and ERAI for December 2006–November 2007 (Fig. 8). These data were obtained from the NASA Langley Research Center CERES ordering tool (http://ceres.larc.nasa.gov/). CERES-EBAF has shown greater accuracy compared to other gridded radiation products as it incorporates detailed cloud and aerosol information (Ma et al. 2015; Wild et al. 2013, 2015; Zhang et al. 2015, 2016). Figure 8 also depicts additional ground-based measurements from independent sites (black dots; Abisko, Sweden; Atqasuk, Alaska; Sondankyla, Finland; and Summit, Greenland) and others that are part of the World Climate Research Programme Baseline Surface Radiation Network (BSRN; Hegner et al. 1998; Ohmura et al. 1998). These stations provide a validation of CERES-EBAF and a comparison between ERAI, ASRv1 (Bromwich et al. 2016), and ASRv2 (Table 3). [For a full description of the radiation data, see Wilson et al. (2012).]

Figure 8a shows ASRv2 SW compared to the CERES-EBAF surface product. In general, ASRv2 has

too much incident SW at the surface across much of the domain, with differences of 20–50 W m^{-2}. Small negative biases (0 to −20 W m^{-2}) are located over the western Arctic Ocean, Hudson Bay, and some parts of Baffin Bay. Conversely, ERAI has generally too much SW compared to the CERES-EBAF over the midlatitudes (Fig. 8b), but too little across the central Arctic where differences exceed 20 W m^{-2}. Comparing these locations to Table 3, differences are consistent between CERES-EBAF and comparisons made at

ground stations. For SW, both ASRv2 and ERAI show an excess of SW, with the greatest differences occurring during the summer months. Though ASRv2 SW biases are greater than ERAI, they are much improved over ASRv1 with a decrease from annual-mean bias of 42 to 27 W m^{-2} in the midlatitudes. Likewise, rmse is lower (95.3 W m^{-2}) and correlations are greater (0.92) than ERAI. Table 3 also supports the findings demonstrated by Figs. 8a and 8b for the polar stations, with too much shortwave radiation in ASRv2
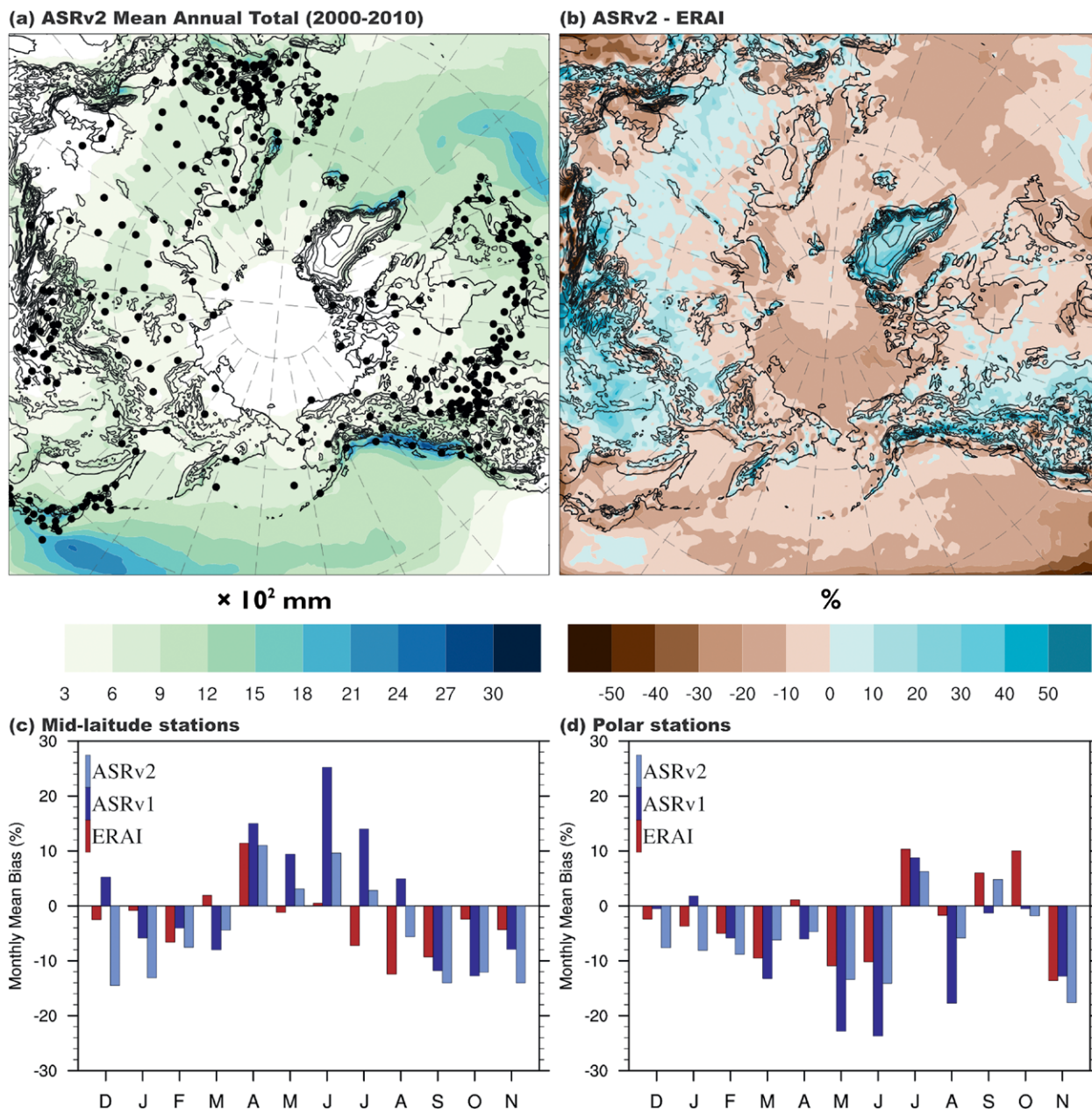

Fɪɢ. 7. (a) ASRv2 mean annual total precipitation (× 10^2 mm) and (b) precipitation difference (%) between ASRv2 and ERAI for the period 2000–10. Black dots in (a) represent station gauges used for (c) midlatitude and (d) polar comparison of monthly precipitation bias (%) for Dec 2006–Nov 2007.

(annual-mean bias of 14.8 W m^{-2}) and too little in ERAI (annual-mean bias of −6.7 W m^{-2}).

Figure 8c shows that ASRv2 generally predicts too little LW radiation across the domain, with differences between CERES-EBAF in the Arctic region ranging from −10 to −20 W m^{-2}. Coupled with Fig. 8a, and despite the improved model cloud physics in Polar WRF, these biases indicate that additional model improvements are necessary in order to fully capture the radiative cloud effects. Comparatively, ERAI produces too much LW over the Arctic Ocean with differences of up to 20 W m^{-2} (Fig. 8d) indicative of too much cloud cover or optically thick clouds in that region.

Comparing these spatial plots to Table 3, again we see consistency as the stations indicate negative LW biases throughout the midlatitudes. ASRv2 improves over both ASRv1 (−11.4 W m^{-2}) and ERAI (−8.8 W m^{-2}) with a mean annual bias of −6.8 W m^{-2}. Unlike the SW, similar negative LW biases occur throughout the year for both ASRv2 and ERAI. In the polar region, consistently low LW biases are evident throughout the annual cycle, and the LW bias in ASRv2 is slightly degraded (−13.9 W m^{-2}) compared to ASRv1 (−11.8 W m^{-2}). Ultimately, these results reflect strongly on the analysis by Hines and Bromwich (2017), who demonstrate that in order to accurately
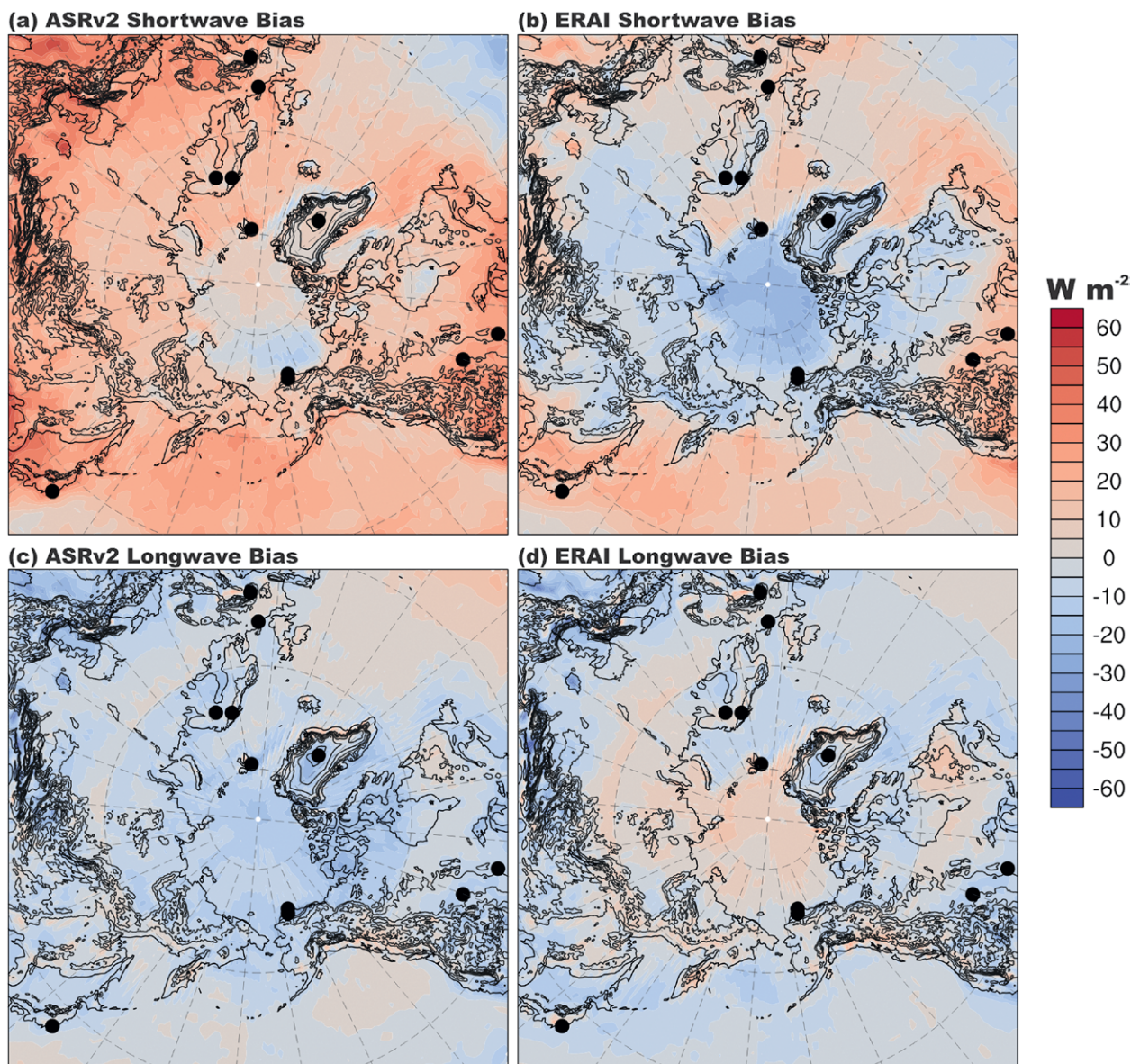

FIG. 8. Bias of annual-mean downward (a),(b) shortwave and (c),(d) longwave radiation (W m^{-2}) at the surface for (a),(c) ASRv2 and (b),(d) ERAI compared to CERES-EBAF satellite product for Dec 2006–Nov 2007.

predict Arctic low clouds, models need accurate cloud condensation nuclei predictions.

CONCLUSIONS. In this paper we have described ASRv2, a new high-resolution regional reanalysis of the greater Arctic covering the period from January 2000 to December 2012. This paper details the production system for ASRv2, including the Polar WRF specifications, WRFDA data assimilation routine, and observational datasets. Noted enhancements over ASRv1 (Bromwich et al. 2016) include increasing the horizontal resolution to 15 km, upgrading Polar WRF

and cloud physics, adding a dual outer-loop routine in the data assimilation to ensure a better fit between the model first guess and observations at analysis time, and additional nudging in the upper levels to remove model biases.

The surface and upper-air analysis fields and forecast precipitation and downward radiation at the surface have been analyzed. Surface analysis with approximately 5,000 surface stations reveals superior comparison in ASRv2, particularly driving down the 10-m wind speed biases and significantly improving the correlations over ASRv1 and ERAI.

TABLE 3. Forecast downward shortwave and longwave radiation at the surface compared to ground stations for Dec 2006–Nov 2007.

Month (No. of stations)	Bias (W m^{-2})			Rmse (W m^{-2})			Correlation		
	ERAI	ASRv1	ASRv2	ERAI	ASRv1	ASRv2	ERAI	ASRv1	ASRv2
Midlatitude stations									
Shortwave									
Dec (5)	4.5	19.6	16.4	61.9	53.4	47.1	0.76	0.90	0.91
Jan (5)	1.6	17.9	13.3	70.3	47.4	43.7	0.79	0.95	0.94
Feb (5)	6.4	26.9	19.7	94.2	68.6	65.5	0.81	0.93	0.92
Mar (5)	21.8	43.8	30.0	130.4	110.5	96.7	0.83	0.92	0.93
Apr (5)	14.5	45.3	36.1	146.9	109.9	98.0	0.87	0.95	0.96
May (5)	20.1	61.5	34.5	152.5	145.9	132.5	0.86	0.92	0.92
Jun (5)	18.0	70.5	38.5	162.8	158.7	145.5	0.85	0.91	0.90
Jul (5)	31.0	70.7	42.7	159.9	156.5	153.4	0.84	0.90	0.87
Aug (5)	22.7	55.8	35.3	145.1	131.5	122.6	0.86	0.92	0.92
Sep (5)	16.3	36.2	20.0	131.2	111.8	101.9	0.84	0.91	0.91
Oct (5)	11.8	31.7	20.1	99.7	90.3	76.0	0.84	0.91	0.93
Nov (5)	6.8	23.5	17.8	70.2	70.2	60.5	0.78	0.88	0.90
Annual	14.6	42.0	27.0	118.8	104.6	95.3	0.83	0.92	0.92
Longwave									
Dec (5)	−9.1	−14.2	−11.9	27.9	32.2	31.0	0.75	0.72	0.73
Jan (5)	−6.5	−12.5	−6.6	25.1	30.0	26.9	0.79	0.78	0.80
Feb (5)	−8.0	−11.0	−6.5	25.4	29.5	27.1	0.82	0.76	0.79
Mar (5)	−10.5	−13.3	−7.4	26.3	28.5	27.1	0.79	0.77	0.79
Apr (5)	−10.9	−12.0	−9.5	22.1	24.5	22.5	0.84	0.80	0.83
May (5)	−9.9	−10.7	−5.8	21.5	23.1	22.3	0.84	0.83	0.82
Jun (5)	−10.3	−12.4	−6.2	23.2	24.7	23.4	0.76	0.75	0.73
Jul (5)	−10.1	−10.8	−6.0	21.2	21.8	21.0	0.81	0.77	0.75
Aug (5)	−8.9	−9.1	−4.2	20.7	22.6	21.2	0.73	0.72	0.75
Sep (5)	−8.9	−8.8	−4.0	20.8	24.2	23.3	0.82	0.76	0.77
Oct (4)	−5.9	−8.9	−5.7	22.2	25.1	24.3	0.81	0.78	0.78
Nov (5)	−7.1	−12.7	−7.9	25.4	29.6	28.3	0.80	0.76	0.78
Annual	−8.8	−11.4	−6.8	23.5	26.3	24.9	0.80	0.77	0.78

TABLE 3. Continued								
	Bias (W m⁻²)			**Rmse (W m⁻²)**			**Correlation**		
Month (No. of stations)	**ERAI**	**ASRv1**	**ASRv2**	**ERAI**	**ASRv1**	**ASRv2**	**ERAI**	**ASRv1**	**ASRv2**
Polar stations									
Shortwave									
Dec (0)									
Jan (4)	−1.1	−0.7	−0.9	2.7	2.1	2.5	0.67	0.69	0.67
Feb (6)	−4.2	1.7	1.7	19.7	13.1	13.9	0.79	0.88	0.87
Mar (6)	−10.0	5.8	9.1	51.9	30.7	35.4	0.86	0.94	0.94
Apr (6)	−18.3	18.2	20.2	77.2	57.9	62.7	0.89	0.95	0.94
May (6)	−1.4	46.7	37.6	93.3	91.8	94.7	0.89	0.92	0.90
Jun (6)	−8.7	37.2	25.5	103.3	111.9	107.4	0.87	0.88	0.88
Jul (6)	−12.3	34.5	34.5	101.1	117.5	116.0	0.85	0.85	0.85
Aug (5)	−9.7	33.0	23.7	77.9	88.5	98.0	0.86	0.87	0.84
Sep (5)	−5.1	16.3	10.9	56.0	54.6	53.9	0.83	0.89	0.88
Oct (5)	−2.2	1.4	0.8	23.3	20.3	21.1	0.79	0.86	0.86
Nov (4)	−1.2	−0.5	−0.8	5.1	3.6	4.0	0.76	0.87	0.86
Annual	−6.7	17.6	14.8	55.6	53.8	55.4	0.82	0.87	0.86
Longwave									
Dec (4)	−10.6	−12.5	−20.5	30.7	36.6	37.9	0.74	0.70	0.71
Jan (4)	−9.6	−8.0	−13.5	31.3	33.4	31.8	0.73	0.69	0.73
Feb (4)	−14.6	−9.7	−14.0	33.2	29.8	30.7	0.72	0.75	0.77
Mar (3)	−6.7	−7.3	−9.1	24.4	26.6	26.9	0.81	0.76	0.72
Apr (3)	−0.4	−17.4	−16.4	26.7	35.7	33.7	0.72	0.71	0.73
May (3)	−11.3	−23.6	−20.5	29.9	41.3	40.3	0.60	0.54	0.55
Jun (3)	2.9	−6.5	−5.7	28.2	35.3	29.6	0.52	0.40	0.51
Jul (3)	0.9	−11.3	−15.4	26.7	33.3	34.1	0.45	0.43	0.37
Aug (2)	2.5	−14.1	−18.7	23.4	32.2	36.5	0.60	0.55	0.54
Sep (2)	−9.7	−16.2	−9.3	27.7	37.0	32.1	0.61	0.48	0.51
Oct (2)	−3.5	0.8	−0.8	24.6	30.9	44.9	0.66	0.47	0.58
Nov (2)	−11.0	−15.9	−22.6	27.3	35.9	37.0	0.70	0.60	0.65
Annual	−5.9	−11.8	−13.9	27.8	34.0	34.6	0.66	0.59	0.61

The upper-air analysis shows an extremely close comparison between ASRv2 and ERAI in 500-hPa temperature and 700-hPa relative humidity, with differences generally within ±0.1°C and ±4%, respectively. Precipitation analysis shows that we have markedly improved summertime precipitation, decreasing the biases during this season by 10%–15%, but a dry bias remains during the cool months. Though comparison between downward radiation at the surface and satellite-derived values reveals that ASRv2 still produces too much shortwave and too little longwave radiation in the forecasts, biases for these values in the midlatitudes are nearly half compared to ASRv1

and the improvement is attributed to the inclusion of subgrid-scale cloud fraction interaction with radiation. Thus, ASRv2 has been shown to be an important synthesis tool for the detection and monitoring of Arctic climate change. (See "Kara and Barents Seas trends" sidebar.) ASRv2 provides important benefits to the research community, in particular those in need of atmospheric data to conduct process studies of Arctic phenomena (e.g., local transport and fluxes) and to drive other environmental models.

Looking forward, of immediate concern is updating ASRv2 beyond 2012 to the present. It is important to continue to capture the accelerated climate changes

Figure SB2a illustrates linear trends in the spatial extent of January sea ice from 2000 to 2012. According to this analysis, the strongest statistically significant trends have occurred in the Kara and Barents Seas around the island of Novaya Zemlya (68°–80°N, 60°–90°E). This is consistent with the analysis by Kohnemann et al. (2017) showing that a reduction of sea ice in this region in late autumn and winter is a driver of enhanced ocean–atmosphere sensible heat flux. The Novaya Zemlya trends for this time period are approximately 40%, nearly 4 times the basinwide sea ice extent decline across the Arctic. Figures SB2b–e show the coupled feedback between this sea ice loss and the atmosphere. Reduced sea ice cover enhances sensible and latent fluxes from the ocean to the atmosphere, leading to an extreme linear change in 2-m temperature over the 13-yr period of nearly 13°C (Fig. SB2b). This energy flux plays a driving role in the evaporation of moisture into the atmospheric boundary layer. Additional moisture in the atmosphere enhances downward longwave radiation at the surface, driving further increases in surface temperature and sea ice melt. Figures SB2c and SB2d support this dynamic relationship with linear changes in downward longwave radiation of 52 to 78 W m^{-2} and specific humidity between 1.04 and 2.08 g kg^{-1} for 2000–12, all statistically significant with p values <0.01. Additionally, the increased moisture leads to significant positive cloud and precipitation trends downwind (and consistent with the mean flow) from the strongest sea ice decline east of Novaya Zemlya (Fig. SB2e). Together, these results demonstrate the capacity to use ASRv2 in a detailed analysis of atmospheric processes associated with surface changes in the Arctic.
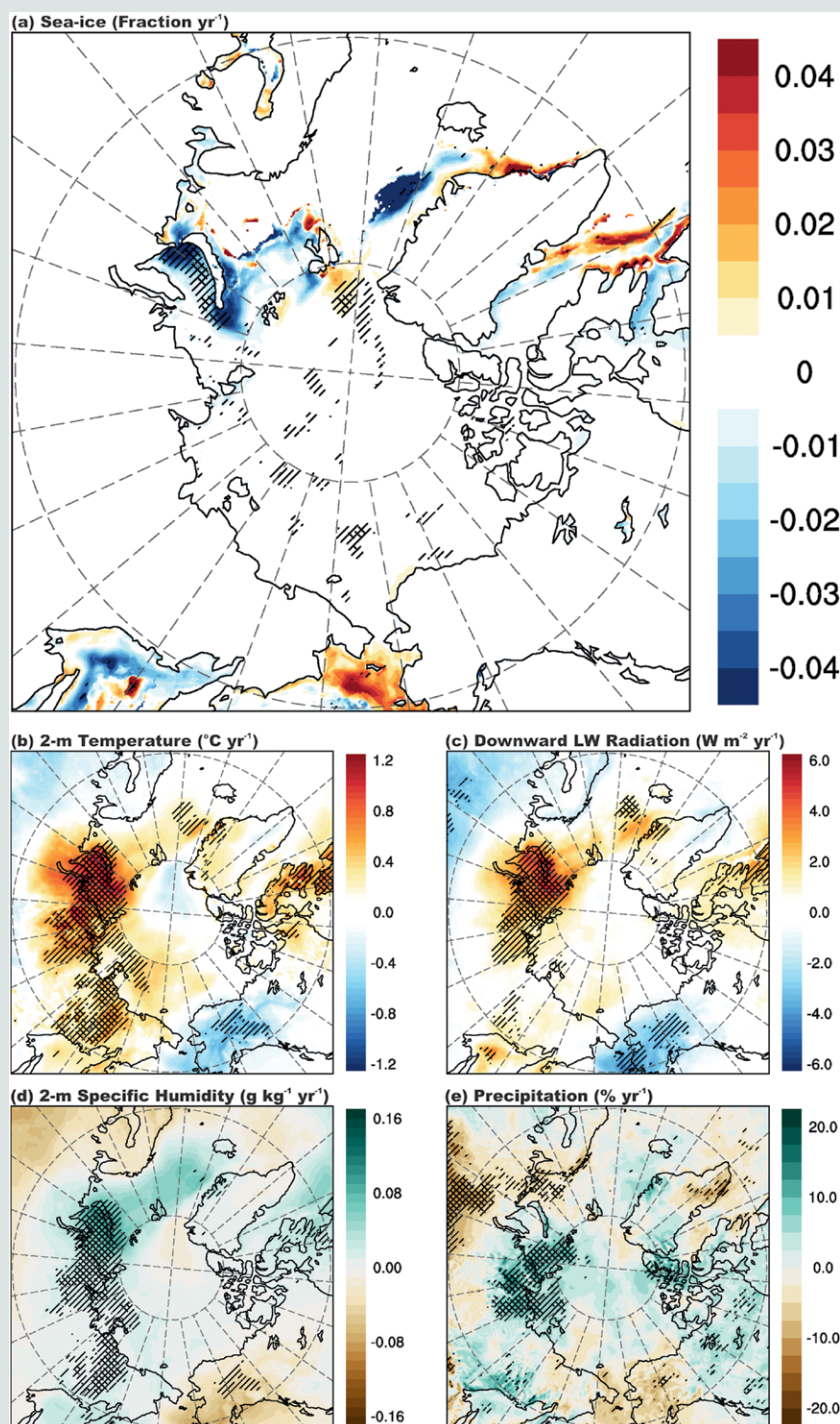
Fig. SB2. Linear Jan trends between 2000 and 2012 in ASRv2 for (a) sea ice fraction, (b) 2-m temperature (°C yr^{-1}), (c) downward surface longwave radiation at the surface (W m^{-2} yr^{-1}), (d) 2-m specific humidity (g kg^{-1} yr^{-1}), and (e) precipitation (% yr^{-1}). Unidirectional hatch marks indicate a p value less than 0.05 and cross-hatch marks indicate p values less than 0.01.

taking place in the Arctic. This includes declining sea ice and snow cover across the Arctic, variables that are likely to be better observed through satellite platforms such as *Cryosat-2* and ICESat-2. Likewise, there is growing support within the Arctic community for an extension of ASR back to 1979 with refinements to the atmosphere, land surface, sea ice modeling, and data assimilation. This will provide a longer context from which to compare the most rapidly changing period in the Arctic to changes that occurred prior to 2000.

REFERENCES

Alapaty, K., J. A. Herwehe, T. L. Otte, C. G. Nolte, O. R. Bullock, M. S. Mallard, J. S. Kain, and J. Dudhia, 2012: Introducing subgrid-scale cloud feedbacks to radiation for regional meteorological and climate modeling. *Geophys. Res. Lett.*, **39**, L24809, https://doi.org/10.1029/2012GL054031.

Auligné, T., A. P. McNally, and D. P. Dee, 2007: Adaptive bias correction for satellite data in a numerical weather prediction system. *Quart. J. Roy. Meteor. Soc.*, **133**, 631–642, https://doi.org/10.1002/qj.56.

Bamber, J. L., S. Ekholm, and W. B. Krabill, 2001: A new, high-resolution digital elevation model of Greenland fully validated with airborne laser altimeter data. *J. Geophys. Res.*, **106**, 6733–6745, https://doi.org/10.1029/2000JB900365.

Barker, D. M., W. Huang, Y.-R. Guo, A. J. Bourgeois, and Q. N. Xiao, 2004: A three-dimensional (3DVAR) data assimilation system for use with MM5: Implementation and initial results. *Mon. Wea. Rev.*, **132**, 897–914, https://doi.org/10.1175/1520-0493(2004)132<0897:ATVDAS>2.0.CO;2.

——, and Coauthors, 2012: The Weather Research and Forecasting Model's Community Variational/Ensemble Data Assimilation System: WRFDA. *Bull. Amer. Meteor. Soc.*, **93**, 831–843, https://doi.org/10.1175/BAMS-D-11-00167.1.

Barlage, M., and Coauthors, 2010: Noah land model modifications to improve snowpack prediction in the Colorado Rocky Mountains. *J. Geophys. Res.*, **115**, D22101, https://doi.org/10.1029/2009JD013470.

Bengtsson, L., and J. Shukla, 1988: Integration of space and in situ observations to study global climate change. *Bull. Amer. Meteor. Soc.*, **69**, 1130–1143, https://doi.org/10.1175/1520-0477(1988)069<1130:IOSAIS>2.0.CO;2.

——, S. Hagemann, and K. I. Hodges, 2004a: Can climate trends be calculated from reanalysis data? *J. Geophys. Res.*, **109**, D11111, https://doi.org/10.1029/2004JD004536.

——, K. I. Hodges, and S. Hagemann, 2004b: Sensitivity of the ERA-40 reanalysis to the observing system: Determination of the global atmospheric circulation from reduced observations. *Tellus*, **56A**, 456–471, https://doi.org/10.3402/tellusa.v56i5.14466.

Bouttier, F., and G. Kelly, 2001: Observing-system experiments in the ECMWF 4D-Var data assimilation system. *Quart. J. Roy. Meteor. Soc.*, **127**, 1469–1488, https://doi.org/10.1002/qj.49712757419.

Bromwich, D. H., K. M. Hines, and L.-S. Bai, 2009: Development and testing of Polar WRF: 2. Arctic Ocean. *J. Geophys. Res.*, **114**, D08122, https://doi.org/10.1029/2008JD010300.

——, A. B. Wilson, L. Bai, G. W. K. Moore, and P. Bauer, 2016: A comparison of the regional Arctic System Reanalysis and the global ERA-Interim reanalysis for the Arctic. *Quart. J. Roy. Meteor. Soc.*, **142**, 644–658, https://doi.org/10.1002/qj.2527.

Chen, F., and J. Dudhia, 2001: Coupling an advanced land surface–hydrology model with the Penn State–NCAR MM5 modeling system. Part I: Model and implementation and sensitivity. *Mon. Wea. Rev.*, **129**, 569–585, https://doi.org/10.1175/1520-0493(2001)129<0569:CAALSH>2.0.CO;2.

Clough, S. A., M. W. Shephard, E. J. Mlawer, J. S. Delamere, M. J. Iacono, K. Cady-Pereira, S. Boukabara, and P. D. Brown, 2005: Atmospheric radiative transfer modeling: A summary of the AER codes. *J. Quant. Spectrosc. Radiat. Transfer*, **91**, 233–244, https://doi.org/10.1016/j.jqsrt.2004.05.058.

Comiso, J., 2003: Warming trends in the Arctic from clear-sky satellite observations. *J. Climate*, **16**, 3498–3510, https://doi.org/10.1175/1520-0442(2003)016<3498:WTITAF>2.0.CO;2.

Cullather, R. I., and M. G. Bosilovich, 2011: The moisture budget of the polar atmosphere in MERRA. *J. Climate*, **24**, 2861–2879, https://doi.org/10.1175/2010JCLI4090.1.

Dee, D. P., and S. M. Uppala, 2009: Variational bias correction of satellite radiance data in the ERA-Interim

reanalysis. *Quart. J. Roy. Meteor. Soc.*, **135**, 1830–1841, https://doi.org/10.1002/qj.493.

——, and Coauthors, 2011: The ERA-Interim reanalysis: Configuration and performance of the data assimilation system. *Quart. J. Roy. Meteor. Soc.*, **137**, 553–597, https://doi.org/10.1002/qj.828.

Derber, J. C., and W.-S. Wu, 1998: The use of TOVS cloud-cleared radiances in the NCEP SSI analysis system. *Mon. Wea. Rev.*, **126**, 2287–2299, https://doi.org/10.1175/1520-0493(1998)126<2287:TUOTCC>2.0.CO;2.

Derksen, C., R. Brown, L. Mudryk, and K. Luojus, 2017: Terrestrial snow cover [in "State of the Climate in 2016"]. *Bull. Amer. Meteor. Soc.*, **98** (8), S93–S98.

Devine, K. A., and È. Mekis, 2008: Field accuracy of Canadian rain measurements. *Atmos.–Ocean*, **46**, 213–227, https://doi.org/10.3137/ao.460202.

Ding, Q., and Coauthors, 2017: Influence of high-latitude atmospheric circulation changes on summertime Arctic sea ice. *Nat. Climate Change*, **7**, 289–295, https://doi.org/10.1038/nclimate3241.

Easterling, D. R., and T. C. Peterson, 1995: A new method for detecting undocumented discontinuities in climatological time series. *Int. J. Climatol.*, **15**, 369–377, https://doi.org/10.1002/joc.3370150403.

Fyfe, J. C., K. von Salzen, N. P. Gillett, V. K. Arora, G. Flato, and J. R. McConnell, 2013: One hundred years of Arctic surface temperature variation due to anthropogenic influence. *Nat. Sci. Rep.*, **3**, 2645, https://doi.org/10.1038/srep02645.

Gelaro, R., and Coauthors, 2017: The Modern-Era Retrospective Analysis for Research and Applications, version 2 (MERRA-2). *J. Climate*, **30**, 5419–5454, https://doi.org/10.1175/JCLI-D-16-0758.1.

Glisan, J. M., W. J. Gutowski, J. J. Cassano, and M. E. Higgins, 2013: Effects of spectral nudging in WRF on Arctic temperature and precipitation simulations. *J. Climate*, **26**, 3985–3999, https://doi.org/10.1175/JCLI-D-12-00318.1.

Hall, D. K., G. A. Riggs, V. V. Salomonson, N. E. DiGirolamo, and K. A. Bayr, 2002: MODIS snow-cover products. *Remote Sens. Environ.*, **83**, 181–194, https://doi.org/10.1016/S0034-4257(02)00095-0.

Han, Y., P. van Delst, Q. Liu, F. Weng, B. Yan, R. Treadon, and J. Derber, 2006: Community Radiative Transfer Model (CRTM): Version 1. NOAA/NESDIS Tech. Rep. 122, 33 pp.

Harig, C., and F. J. Simons, 2016: Ice mass loss in Greenland, the Gulf of Alaska, and the Canadian Archipelago: Seasonal cycles and decadal trends. *Geophys. Res. Lett.*, **43**, 3150–3159, https://doi.org/10.1002/2016GL067759.

Hartmann, B., and G. Wendler, 2005: The significance of the 1976 Pacific climate shift in the climatology of Alaska. *J. Climate*, **18**, 4824–4839, https://doi.org/10.1175/JCLI3532.1.

Hegner, H., G. Müller, V. Nespor, A. Ohmura, R. Steigrad, and H. Gilgen, 1998: World Climate Research Program WCRP (WMO/ICSU/IOC) Baseline Surface Radiation Network (BSRN): Update of the technical plan for BSRN data management, version 1.0. World Radiation Monitoring Center Tech. Rep. 2, 38 pp.

Hines, K. M., and D. H. Bromwich, 2008: Development and testing of Polar Weather Research and Forecasting (WRF) Model. Part I: Greenland Ice Sheet meteorology. *Mon. Wea. Rev.*, **136**, 1971–1989, https://doi.org/10.1175/2007MWR2112.1.

——, and ——, 2017: Simulation of late summer Arctic clouds during ASCOS with Polar WRF. *Mon. Wea. Rev.*, **145**, 521–541, https://doi.org/10.1175/MWR-D-16-0079.1.

——, ——, L.-S. Bai, M. Barlage, and A. S. Slater, 2011: Development and testing of Polar WRF. Part III: Arctic land. *J. Climate*, **24**, 26–48, https://doi.org/10.1175/2010JCLI3460.1.

——, ——, ——, C. M. Bitz, J. G. Powers, and K. W. Manning, 2015: Sea ice enhancements to Polar WRF. *Mon. Wea. Rev.*, **143**, 2363–2385, https://doi.org/10.1175/MWR-D-14-00344.1.

Huang, X.-Y., and Coauthors, 2009: Four-dimensional variational data assimilation for WRF: Formulation and preliminary results. *Mon. Wea. Rev.*, **137**, 299–314, https://doi.org/10.1175/2008MWR2577.1.

Iacono, M. J., J. S. Delamere, E. J. Mlawer, M. W. Shepard, S. A. Clough, and W. D. Collins, 2008: Radiative forcing by long-lived greenhouse gases: Calculations with the AER radiative transfer models. *J. Geophys. Res.*, **113**, D13103, https://doi.org/10.1029/2008JD009944.

Intergovernmental Panel on Climate Change, 2013: *Climate Change 2013: The Physical Science Basis*. Cambridge University Press, 1535 pp.

Jakobson, E., T. Vihma, T. Palo, L. Jakobson, H. Keernik, and J. Jaagus, 2012: Validation of atmospheric reanalyses over the central Arctic Ocean. *Geophys. Res. Lett.*, **39**, L10802, https://doi.org/10.1029/2012GL051591.

Jiang, L., D. Tarpley, K. E. Mitchell, S. Zhou, F. N. Kogan, and W. Guo, 2008: Adjusting for long-term anomalous trends in NOAA's Global Vegetation Index data sets. *IEEE Trans. Geosci. Remote Sens.*, **46**, 409–422, https://doi.org/10.1109/TGRS.2007.902844.

Jung, T., and Coauthors, 2016: Advancing polar prediction capabilities on daily to seasonal time scales.

Bull. Amer. Meteor. Soc., **97**, 1631–1647, https://doi .org/10.1175/BAMS-D-14-00246.1.

Kain, J. S., 2004: The Kain-Fritsch convective parameterization: An update. *J. Appl. Meteor.*, **43**, 170–181, https://doi.org/10.1175/1520-0450(2004)043<0170: TKCPAU>2.0.CO;2.

——, and J. M. Fritsch, 1990: A one-dimensional entraining/detraining plume model and its application in convective parameterization. *J. Atmos. Sci.*, **47**, 2784–2802, https://doi.org/10.1175/1520 -0469(1990)047<2784:AODEPM>2.0.CO;2.

——, and ——, 1993: Convective parameterization for mesoscale models: The Kain–Fritsch scheme. *The Representation of Cumulus Convection in Numerical Models*, *Meteor. Monogr.*, No. 46, Amer. Meteor. Soc., 165–170.

Kato, S., N. G. Loeb, F. G. Rose, D. R. Doelling, D. A. Rutan, T. E. Caldwell, L. Yu, and R. A. Weller, 2013: Surface irradiances consistent with CERES-derived top-of-atmosphere shortwave and longwave irradiances. *J. Climate*, **26**, 2719–2740, https://doi .org/10.1175/JCLI-D-12-00436.1.

Kay, J. E., M. M. Holland, and A. Jahn, 2011: Interannual to multi-decadal Arctic sea ice extent trends in a warming world. *Geophys. Res. Lett.*, **38**, L15708, https://doi.org/10.1029/2011GL048008.

Kohnemann, S. H. E., G. Heinemann, D. H. Bromwich, and O. Gutjahr, 2017: Extreme warming in the Kara Sea and Barents Sea during the winter period 2000–16. *J. Climate*, 30, 8913–8927, https://doi.org/10.1175 /JCLI-D-16-0693.1.

Kwok, R., and N. Untersteiner, 2011: The thinning of Arctic sea ice. *Phys. Today*, **64**, 36–41, https://doi .org/10.1063/1.3580491.

Lenaerts, J. T. M., J. H. van Angelen, M. R. van den Broeke, A. S. Gardner, B. Wouters, and E. van Meijgaard, 2013: Irreversible mass loss of Canadian Arctic Archipelago glaciers. *Geophys. Res. Lett.*, **40**, 870–874, https://doi.org/10.1002/grl.50214.

L'Heureux, M. L., A. Kumar, G. D. Bell, M. S. Halpert, and R. W. Higgins, 2008: Role of the Pacific–North American (PNA) pattern in the 2007 Arctic sea ice decline. *Geophys. Res. Lett.*, **35**, L20701, https://doi .org/10.1029/2008GL035205.

Lindsay, R., M. Wensnahan, A. Schweiger, and J. Zhang, 2014: Evaluation of seven different atmospheric reanalysis products in the Arctic. *J. Climate*, **27**, 2588–2606, https://doi.org/10.1175/JCLI-D-13 -00014.1.

Liu, Z., C. S. Schwartz, C. Snyder, and S. Ha, 2012: Impact of assimilating AMSU-A radiances on forecasts of 2008 Atlantic tropical cyclones initialized with a limited-area ensemble Kalman filter. *Mon.*

Wea. Rev., **140**, 4017–4034, https://doi.org/10.1175 /MWR-D-12-00083.1.

Loeb, N. G., B. A. Wielicki, D. R. Doelling, G. Smith, D. F. Keyes, S. Kato, N. Manalo-Smith, and T. Wong, 2009: Toward optimal closure of the Earth's top-of-atmosphere radiation budget. *J. Climate*, **22**, 748–766, https://doi.org/10.1175/2008JCLI2637.1.

Ma, Q., K. C. Wang, and M. Wild, 2015: Impact of geolocations of validation data on the evaluation of surface incident shortwave radiation from earth system models. *J. Geophys. Res. Atmos.*, **120**, 6825–6844, https://doi.org/10.1002/2014JD022572.

Maslanik, J. A., C. Fowler, J. Stroeve, S. Drobot, J. Zwally, D. Yi, and W. Emery, 2007: A younger, thinner Arctic ice cover: Increased potential for rapid, extensive sea-ice loss. *Geophys. Res. Lett.*, **34**, L24501, https:// doi.org/10.1029/2007GL032043.

——, J. Stroeve, C. Fowler, and W. Emery, 2011: Distribution and trends in Arctic sea ice age through spring 2011. *Geophys. Res. Lett.*, **38**, L13502, https:// doi.org/10.1029/2011GL047735.

Mekis, È., 2005: Adjustments for trace measurements in Canada. *15th Conf. on Applied Climatology/13th Symp. on Meteorological Observations and Instrumentation,* Savannah, GA, Amer. Meteor. Soc., J3.7, https://ams.confex.com/ams/15AppClimate /techprogram/paper_92155.htm.

——, and W. D. Hogg, 1999: Rehabilitation and analysis of Canadian daily precipitation time series. *Atmos.–Ocean*, **37**, 53–85, https://doi.org/10.1080/07055900 .1999.9649621.

——, and R. Hopkinson, 2004: Derivation of an improved snow water equivalent adjustment factor map for application on snowfall ruler measurements in Canada. *Proc. 14th Conf. on Applied Climatology*, Seattle, WA, Amer. Meteor. Soc., 7.12, https://ams.confex.com /ams/84Annual/techprogram/paper_68724.htm.

Moore, G. W. K., D. H. Bromwich, A. B. Wilson, I. Renfrew, and L. Bai, 2016: Arctic System Reanalysis improvements in topographically-forced winds near Greenland. *Quart. J. Roy. Meteor. Soc.*, **142**, 2033–2045, https://doi.org/10.1002/qj.2798.

Nakanishi, M., 2001: Improvement of the Mellor–Yamada turbulence closure model based on large-eddy simulation data. *Bound.-Layer Meteor.*, **99**, 349–378, https://doi.org/10.1023/A:1018915827400.

——, and H. Niino, 2004: An improved Mellor–Yamada level-3 model with condensation physics: Its design and verification. *Bound.-Layer Meteor.*, **112**, 1–31, https://doi.org/10.1023/B:BOUN.0000020164 .04146.98.

——, and ——, 2006: An improved Mellor–Yamada level-3 model: Its numerical stability and application

to a regional prediction of advection fog. *Bound.-Layer Meteor.*, **119**, 397–407, https://doi.org/10.1007/s10546-005-9030-8.

National Center for Atmospheric Research/University Corporation for Atmospheric Research, and Polar Meteorology Group/Byrd Polar and Climate Research Center/The Ohio State University, 2017: Arctic System Reanalysis version 2. Research Data Archive at the National Center for Atmospheric Research, Computational and Information Systems Laboratory, Boulder, CO, https://doi.org/10.5065/D6X9291B.

National Oceanic and Atmospheric Administration, 2016: Arctic Report Card. Accessed 27 April 2017, http://arctic.noaa.gov/Report-Card.

National Snow and Ice Data Center, 2017: Arctic sea ice news and analysis. Accessed 27 April 2017, http://nsidc.org/arcticseaicenews/.

Nghiem, S. V., and Coauthors, 2012: The extreme melt across the Greenland ice sheet in 2012. *Geophys. Res. Lett.*, **39**, L20502, https://doi.org/10.1029/2012GL053611.

Ohmura, A., and Coauthors, 1998: Baseline Surface Radiation Network (BSRN/WCRP): New precision radiometry for climate research. *Bull. Amer. Meteor. Soc.*, **79**, 2115–2136, https://doi.org/10.1175/1520-0477(1998)079<2115:BSRNBW>2.0.CO;2.

Overland, J. E., and M. Wang, 2005: The Arctic climate paradox: The recent decrease of the Arctic Oscillation. *Geophys. Res. Lett.*, **32**, L06701, https://doi.org/10.1029/2004GL021752.

Pan, M., and Coauthors, 2003: Snow process modeling in the North American Land Data Assimilation System (NLDAS): 2. Evaluation of model simulated snow water equivalent. *J. Geophys. Res.*, **108**, 8850, https://doi.org/10.1029/2003JD003994.

Parrish, D. F., and J. C. Derber, 1992: The National Meteorological Center's spectral statistical-interpolation analysis system. *Mon. Wea. Rev.*, **120**, 1747–1763, https://doi.org/10.1175/1520-0493(1992)120<1747:TNMCSS>2.0.CO;2.

Peterson, T. C., and D. R. Easterling, 1994: Creation of homogeneous composite climatological reference series. *Int. J. Climatol.*, **14**, 671–679, https://doi.org/10.1002/joc.3370140606.

——, and R. S. Vose, 1997: An overview of the Global Historical Climatology Network temperature database. *Bull. Amer. Meteor. Soc.*, **78**, 2837–2849, https://doi.org/10.1175/1520-0477(1997)078<2837:AOOTGH>2.0.CO;2.

Powers, J. G., K. W. Manning, D. H. Bromwich, J. J. Cassano, and A. M. Cayette, 2012: A decade of Antarctic science support through AMPS. *Bull.*

Amer. Meteor. Soc., **93**, 1699–1712, https://doi.org/10.1175/BAMS-D-11-00186.1.

——, and Coauthors, 2017: The Weather Research and Forecasting Model: Overview, system efforts, and future directions. *Bull. Amer. Meteor. Soc.*, **98**, 1717–1737, https://doi.org/10.1175/BAMS-D-15-00308.1.

Rienecker, M. M., and Coauthors, 2011: MERRA: NASA's Modern-Era Retrospective Analysis for Research and Applications. *J. Climate*, **24**, 3624–3648, https://doi.org/10.1175/JCLI-D-11-00015.1.

Rignot, E., I. Velicogna, M. R. van den Broeke, A. Monaghan, and J. T. M. Lenaerts, 2011: Acceleration of the contribution of the Greenland and Antarctic ice sheets to sea level rise. *Geophys. Res. Lett.*, **38**, L05503, https://doi.org/10.1029/2011GL047109.

Rigor, I. G., and J. M. Wallace, 2004: Variations in the age of Arctic sea-ice and summer sea-ice extent. *Geophys. Res. Lett.*, **31**, L09401, https://doi.org/10.1029/2004GL019492.

Rogers, A. N., D. H. Bromwich, E. N. Sinclair, and R. I. Cullather, 2001: The atmospheric hydrologic cycle over the Arctic basin from reanalyses. Part II: Interannual variability. *J. Climate*, **14**, 2414–2429, https://doi.org/10.1175/1520-0442(2001)014<2414:TAHCOT>2.0.CO;2.

Romanovsky, V. E., S. L. Smith, and H. H. Christiansen, 2010: Permafrost thermal state in the polar Northern Hemisphere during the International Polar Year 2007–2009: A synthesis. *Permafrost Periglacier Processes*, **21**, 105–116, https://doi.org/10.1002/ppp.689.

Saha, S., and Coauthors, 2010: The NCEP Climate Forecast System Reanalysis. *Bull. Amer. Meteor. Soc.*, **91**, 1015–1057, https://doi.org/10.1175/2010BAMS3001.1.

Samelson, R. M., and P. L. Barbour, 2008: Low-level jets, orographic effects, and extreme events in Nares Strait: A model-based mesoscale climatology. *Mon. Wea. Rev.*, **136**, 4746–4759, https://doi.org/10.1175/2007MWR2326.1.

Schaaf, C. B., and Coauthors, 2002: First operational BRDF, albedo and nadir reflectance products from MODIS. *Remote Sens. Environ.*, **83**, 135–148, https://doi.org/10.1016/S0034-4257(02)00091-3.

Schwartz, C. S., Z. Liu, Y. Chen, and X.-Y. Huang, 2012: Impact of assimilating microwave radiances with a limited-area ensemble data assimilation system on forecasts of Typhoon Morakot. *Wea. Forecasting*, **27**, 424–437, https://doi.org/10.1175/WAF-D-11-00033.1.

Screen, J. A., and I. Simmonds, 2010: The central role of diminishing sea ice in recent Arctic temperature amplification. *Nature*, **464**, 1334–1337, https://doi.org/10.1038/nature09051.

——, C. Deser, and I. Simmonds, 2012: Local and remote controls on observed Arctic warming. *Geophys. Res. Lett.*, **39**, L10709, https://doi.org/10.1029/2012GL051598.

Serreze, M. C., and A. P. Barrett, 2011: Characteristics of the Beaufort Sea high. *J. Climate*, **24**, 159–182, https://doi.org/10.1175/2010JCLI3636.1.

——, and J. Francis, 2006: The Arctic amplification debate. *Climatic Change*, **76**, 241–264, https://doi.org/10.1007/s10584-005-9017-y.

Skamarock, W. C., and Coauthors, 2008: A description of the Advanced Research WRF version 3. NCAR Tech. Note NCAR/TN-475+STR, 113 pp., https://doi.org/10.5065/D68S4MVH.

Slater, A. G., T. J. Bohn, J. L. McCreight, M. C. Serreze, and D. P. Lettenmaier, 2007: A multimodel simulation of pan-Arctic hydrology. *J. Geophys. Res.*, **112**, G04S45, https://doi.org/10.1029/2006JG000303.

Stöckli, R., E. Vermote, N. Saleous, R. Simmon, and D. Herring, 2005: The Blue Marble Next Generation: A true color Earth dataset including seasonal dynamics from MODIS. NASA Earth Observatory, accessed 26 April 2017, https://earthobservatory.nasa.gov/Features/BlueMarble/?src=ve.

Tao, W.-K., and J. Simpson, 1993: The Goddard Cumulus Ensemble model. Part I. Model description. *Terr. Atmos. Ocean. Sci.*, **4**, 19–54, https://doi.org/10.3319/TAO.1993.4.1.35(A).

——, and Coauthors, 2003: Microphysics, radiation and surface processes in the Goddard Cumulus Ensemble (GCE) model. *Meteor. Atmos. Phys.*, **82**, 97–137, https://doi.org/10.1007/s00703-001-0594-7.

Thompson, D. W. J., and J. M. Wallace, 2000: Annular modes in the extratropical circulation. Part I: Month-to-month variability. *J. Climate*, **13**, 1000–1016, https://doi.org/10.1175/1520-0442(2000)013<1000:AMITEC>2.0.CO;2.

Tilinina, N., S. K. Gulev, and D. H. Bromwich, 2014: New view of Arctic cyclone activity from the Arctic system reanalysis. *Geophys. Res. Lett.*, **41**, 1766–1772, https://doi.org/10.1002/2013GL058924.

Tilling, R. L., A. Ridout, A. Shepherd, and D. J. Wingham, 2015: Increased Arctic sea ice volume after anomalously low melting in 2013. *Nat. Geosci.*, **8**, 643–646, https://doi.org/10.1038/ngeo2489.

Walsh, J. E., F. Fetterer, J. S. Stewart, and W. L. Chapman, 2017: Database for depicting Arctic sea ice variations back to 1850. *Geogr. Rev.*, **107**, 89–107, https://doi.org/10.1111/j.1931-0846.2016.12195.x.

Wild, M., D. Folini, C. Schär, N. Loeb, E. Dutton, and G. König-Langlo, 2013: The global energy balance from a surface perspective. *Climate Dyn.*, **40**, 3107–3134, https://doi.org/10.1007/s00382-012-1569-8.

——, and Coauthors, 2015: The energy balance over land and oceans: An assessment based on direct observations and CMIP5 climate models. *Climate Dyn.*, **44**, 3393–3429, https://doi.org/10.1007/s00382-014-2430-z.

Wilson, A. B., D. H. Bromwich, and K. M. Hines, 2011: Evaluation of Polar WRF forecasts on the Arctic System Reanalysis domain: Surface and upper air analysis. *J. Geophys. Res.*, **116**, D11112, https://doi.org/10.1029/2010JD015013.

——, D. H. Bromwich, and K. M. Hines, 2012: Evaluation of Polar WRF forecasts on the Arctic System Reanalysis domain: 2. Atmospheric hydrologic cycle. *J. Geophys. Res.*, **117**, D04107, https://doi.org/10.1029/2011JD016765.

Zhang, L., A. Kumar, and W. Wang, 2012: Influence of changes in observations on precipitation: A case study for the Climate Forecast System Reanalysis (CFSR). *J. Geophys. Res.*, **117**, D08105, https://doi.org/10.1029/2011JD017347.

Zhang, X., S. Liang, M. Wild, and B. Jiang, 2015: Analysis of surface incident shortwave radiation from four satellite products. *Remote Sens. Environ.*, **165**, 186–202, https://doi.org/10.1016/j.rse.2015.05.015.

——, ——, G. Wang, Y. Yao, B. Jiang, and J. Cheng, 2016: Evaluation of the reanalysis surface incident shortwave radiation products from NCEP, ECMWF, GSFC, and JMA using satellite and surface observations. *Remote Sens.*, **8**, 225, https://doi.org/10.3390/rs8030225.

Zheng, Y., K. Alapaty, J. A. Herwehe, A. D. Del Genio, and D. Niyogi, 2016: Improving high-resolution weather forecasts using the Weather Research and Forecasting (WRF) Model with an updated Kain–Fritsch scheme. *Mon. Wea. Rev.*, **144**, 833–860, https://doi.org/10.1175/MWR-D-15-0005.1.

AMS BOOKS

**RESEARCH ◆ APPLICATIONS ◆ HISTORY**

CLIMATE

The Thinking Person's Guide to Climate Change

ROBERT HENSON

This fully updated and expanded revision of The *Rough Guide to Climate Change* combines years of data with recent research. It is the most comprehensive overview of climate science, acknowledging controversies but standing strong in its stance that the climate is changing—and something needs to be done.

© 2014, PAPERBACK, 520 PAGES,
ISBN: 978-1-935704-73-7
LIST $30   MEMBER $20

BEST SELLER!
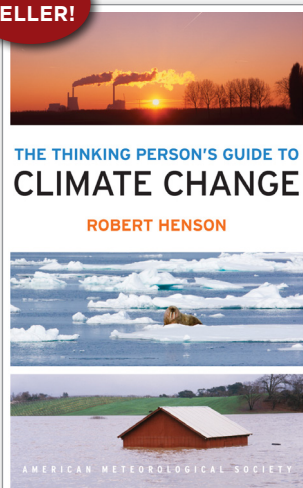
Climate Conundrums: What the Climate Debate Reveals about Us

WILLIAM B. GAIL

This is a journey through how we think, individually and collectively, about humanity's relationship with nature, and more. Can we make nature better? Could science and religion reconcile? Gail's insights on such issues help us better understand who we are and find a way forward.

© 2014, PAPERBACK, 240 PAGES,
ISBN: 978-1-935704-74-4   **LIST $30   MEMBER $20**

Living on the Real World: How Thinking and Acting Like Meteorologists Will Help Save the Planet

WILLIAM H. HOOKE

Meteorologists focus on small bits of information while using frequent collaboration to make decisions. With climate change a reality, William H. Hooke suggests we look to the way meteorologists operate as a model for how we can solve the 21st century's most urgent environmental problems.

© 2014, PAPERBACK, 272 PAGES, ISBN 978-1-935704-56-0   **LIST $30   MEMBER $22**
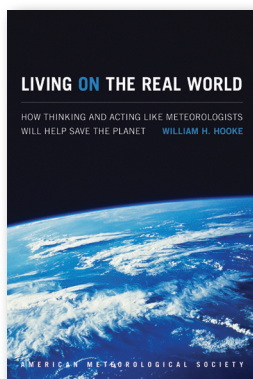
Synoptic-Dynamic Meteorology Lab Manual:

Visual Exercises to Complement Midlatitude Synoptic Meteorology

GARY LACKMANN, BRIAN E. MAPES, AND KEVIN R. TYLE

These labs link theoretical concepts with ground-breaking visualization to elucidate concepts taught in the award-winning companion textbook by Gary Lackmann, *Midlatitude Synoptic Meteorology.*

© 2017, PAPERBACK, 126 PAGES,
ISBN 978-1-878220-26-4

LIST $80   MEMBER $60   STUDENT $50

AWARD WINNER!
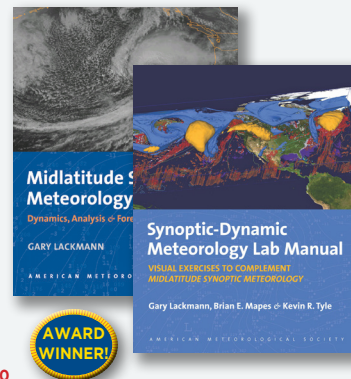
GUIDES

An Observer's Guide to Clouds and Weather:

A Northeastern Primer on Prediction

TOBY CARLSON, PAUL KNIGHT, AND CELIA WYCKOFF

With help from Penn State experts, start at the beginning and go deep. This primer, intended for both serious enthusiasts and new meteorology students, will leave you with both refined observation skills and an understanding of the complex science behind the weather: the ingredients for making reliable predictions of your own. It connects fundamental meteorological concepts with the processes that shape weather patterns, and will make an expert of any dedicated reader.

© 2014, PAPERBACK, 210 PAGES,
ISBN: 978-1-935704-58-4   **LIST $30   MEMBER $20**
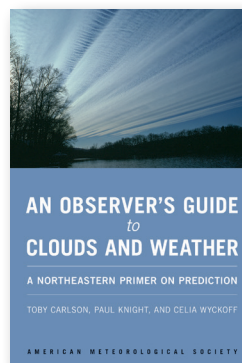
Eloquent Science:

A Practical Guide to Becoming a Better Writer, Speaker, and Atmospheric Scientist

DAVID M. SCHULTZ

The ultimate communications manual for undergraduate and graduate students as well as researchers in the atmospheric sciences and their intersecting disciplines.

© 2009, PAPERBACK, 440 PAGES,
ISBN 978-1-878220-91-2

LIST $45   MEMBER $30

AWARD WINNER!
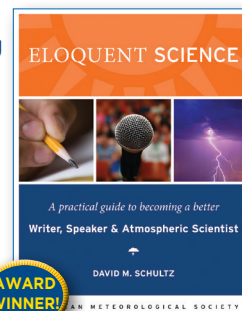
To order: bookstore.ametsoc.org, 617-226-3998, or use the order form in this magazine

NEW

Verner Suomi: The Life and Work of the Founder of Satellite Meteorology

JOHN M. LEWIS WITH JEAN M. PHILLIPS, W. PAUL MENZEL, THOMAS H. VONDER HAAR, HANS MOOSMÜLLER, FREDERICK B. HOUSE, AND MATTHEW G. FEARON

Born in a Minnesotan mining town, Suomi would spend his best years next door in Wisconsin, but not before seeing the whole world—from space, that is. This is the story of the scientist, inventor, and teacher who founded satellite meteorology, written by members of the communities that grew up around his groundbreaking work.

LIST $30   MEMBER $20

© 2016, PAPERBACK, 240 PAGES, ISBN: 978-1-944970-22-2
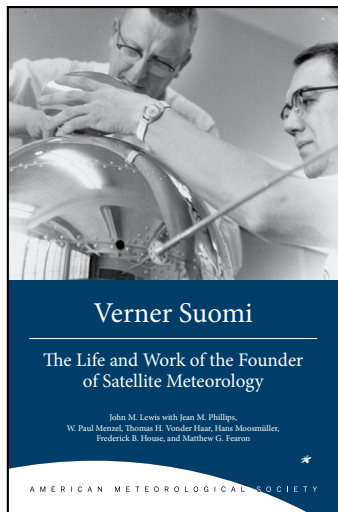
Weather in the Courtroom: Memoirs from a Career iForensic Meteorology
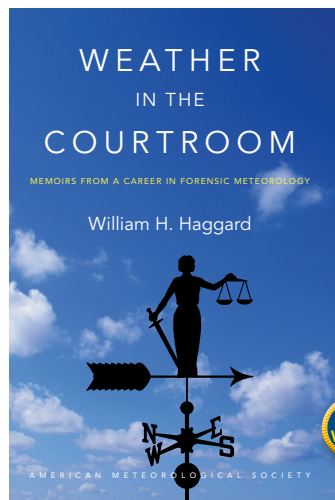
WILLIAM H. HAGGARD

From a pioneering forensic meteorologist, the inside scoop on legendary litigations, including the disappearance of an Alaskan congressman's airplane in 1972, the collapse of Tampa Bay's Skyway Bridge in 1980, and the crash of Delta Flight 191 in Dallas/Fort Worth in 1985.

LIST $30   MEMBER $20
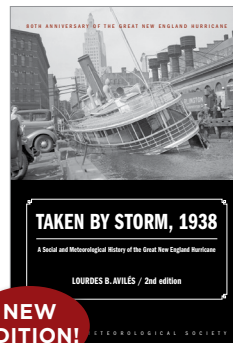
© 2016, PAPERBACK, 240 PAGES, ISBN: 978-1-940033-95-2

AWARD WINNER!

![AMS American Meteorological Society logo]

Booksellers, groups, or for examination copies:
The University of Chicago Press:
1-800-621-2736 (US & Canada)
773-702-7000 (all others)
custserv@press.uchicago.edu

HISTORY

Taken by Storm, 1938: A Social and Meteorological History of the Great New England Hurricane, 2nd Ed.

LOURDES B. AVILÉS

80TH ANNIVERSARY OF STORM

NEW EDITION!

The science behind the 1938 Hurricane, which hit New England unannounced, is presented here for the first time along with new data that sheds light on the motivations of the Weather Bureau forecasters. This compelling history successfully weaves science, historical accounts, and social analyses to create a comprehensive picture of the most powerful and devastating hurricane to hit New England to date.

© 2018, PAPERBACK, 288 PAGES, ISBN: 978-1-944970-24-6

LIST $30   MEMBER $20

A Scientific Peak: How Boulder Became a World Center for Space and Atmospheric Science

JOSEPH P. BASSI

How did big science come to Boulder, Colorado? Joe Bassi introduces us to the characters, including Harvard sun–Earth researcher Walter Orr Roberts, and the unexpected brew of politics, passion, and sheer luck that during the Cold War era transformed this "Scientific Siberia" to home of NCAR and NOAA.
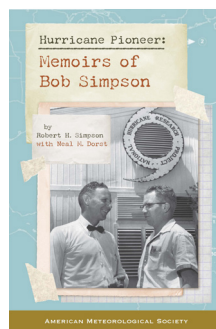
© 2015, PAPERBACK, 264 PAGES, ISBN: 978-1-935704-85-0

LIST PRICE: $35.00   MEMBER PRICE: $25.00
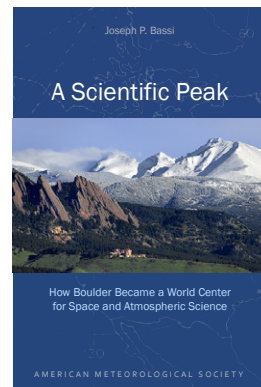
Hurricane Pioneer: Memoirs of Bob Simpson

ROBERT H. SIMPSON AND NEAL DORST

In 1951, Bob Simpson rode a plane into a hurricane—just one of the many pioneering exploits you'll find in these memoirs. Bob and his wife Joanne are meteorological icons: Bob was the first director of the National Hurricane Research Project and a director of the National Hurricane Center. He helped to create the Saffir–Simpson Hurricane Scale; the public knows well his Categories 1–5. Proceeds from this book help support the AMS's K. Vic Ooyama Scholarship Fund.

© 2015, PAPERBACK, 156 PAGES
ISBN: 978-1-935704-75-1   LIST $25   MEMBER $20

AMS 100th Anniversary Campaign

**Imagine the potential
Engage the world
Empower the future**

Why I want to Leave a Legacy Gift to AMS

> "I have benefitted from the diversity of communities working in atmospheric sciences. This rich interdisciplinary mix has encouraged me to remain current—including in areas outside my specific expertise—and has provided me with networking opportunities in many fields."

A member since graduate school, Susan Avery quickly discovered that AMS helped shape her future. Susan wanted to give back to the Society. She and her husband Jim were able to give far more than they first envisioned by designating AMS as a beneficiary of their retirement plans.

There are many—surprisingly easy—ways to give. Read more giving stories at www.ametsoc.org: click the red "donate" button.

In 2019, we celebrate 100 years of service to our profession. Your support will help AMS launch new initiatives to expand its diversity; strengthen and grow the weather, water, and climate community; foster public education, and deepen our impact on science and on society.

ametsoc.org/give

Please consider donating to any of the five key areas of the Campaign.
Rapid Adaptation | Breakthrough Science | Engaging the Public | Bridging Disciplines | Globalization